A multi-omics analysis of human fibroblasts overexpressing an *Alu* transposon reveals widespread disruptions in aging-associated pathways

Juan I. Bravo,[1,8] Eyael Tewelde,[2,3,8] Christina D. King,[4] Joanna Bons,[4] Samah Shah,[4] Jacob Rose,[4] Judith Campisi,[4] Birgit Schilling,[4] and Bérénice A. Benayoun[1,2,5,6,7,9,*]

[1]Leonard Davis School of Gerontology, University of Southern California, Los Angeles, CA 90089, USA.

[2]Alfred E. Mann School of Pharmacy and Pharmaceutical Sciences, University of Southern California, Los Angeles, CA 90033, USA.

[3]Graduate program in Pharmaceutical and Translational Sciences, University of Southern California, Los Angeles, CA 90033, USA.

[4]Buck Institute for Research on Aging, Novato, CA 94945, USA.

[5] Cancer Biology Department, USC Keck School of Medicine, Los Angeles, CA 90033, USA.

[6]USC Norris Comprehensive Cancer Center, Epigenetics and Gene Regulation, Los Angeles, CA 90033, USA.

[7]USC Stem Cell Initiative, Los Angeles, CA 90089, USA.

[8]These authors contributed equally

[9]Lead contact

*Correspondence: bbenayou@usc.edu

SUMMARY

During aging and cellular senescence, repetitive elements are frequently transcriptionally derepressed across species and cell types. Among these, the most abundant repeats by copy number in the human genome are *Alu* retrotransposons. Though *Alu* elements are often studied for their mutagenic potential, there is increasing appreciation for their contributions to other biological functions, including pro-inflammatory signaling and mitochondrial dysfunction. However, a comprehensive analysis of *Alu*-driven molecular changes remains to be conducted, and *Alu*'s potential contributions to aging features remain incompletely characterized. Here, we show that overexpression of an *AluJb* transposon in human primary IMR-90 fibroblasts leads to large-scale alterations across the transcriptome, cellular proteome, and secretome. Functional genomics analyses reveal alterations in aging/senescence pathways, broadly, and mitochondrial metabolism, proteostasis, cell cycle, and extracellular matrix pathways, more specifically. Our results demonstrate that *Alu* transcriptional upregulation is sufficient to drive widespread disruptions to cellular homeostasis that mirror aging-associated alterations.

KEYWORDS

Aging, Retrotransposons, *Alu*, Fibroblasts, Mitochondria, Cell Cycle, Proteostasis, Transcriptomics, Proteomics, Secretome

INTRODUCTION

Transposable elements (TEs), often informally referred to as “jumping genes”, are genetic elements that can mobilize within a genome. Depending on mobilization mechanisms, TEs can be classified as DNA transposons, which operate through a “cut-and-paste” mechanism, or retrotransposons, which operate through a “copy-and-paste” mechanism (Kidwell, 2002). Historically, transposable elements have been largely ignored in biological studies because of (1) biases that considered TEs “junk” DNA and (2) the extreme difficulty of working with multi-copy, highly repetitive genomic sequences. Thus, there is frequently a gap in our understanding of the relationship between TEs and biological processes of interest, such as cellular senescence or aging.

Technological advancements over the past two decades (including next generation sequencing) have facilitated the study of TEs, including in the context of aging and aging-associated diseases [reviewed in (Bravo et al., 2020)]. For example, age-related de-repression of TEs has been observed across diverse model systems, including *Caenorhabditis elegans* (Dennis et al., 2012), *Drosophila* (Chen et al., 2016; Li et al., 2013; Wood et al., 2016), and *Mus musculus* (Benayoun et al., 2018; De Cecco et al., 2013b), and in senescent cells (De Cecco et al., 2013a; De Cecco et al., 2019; Wang et al., 2011). Importantly, TE de-repression has also been observed across age-associated pathologies, e.g. cell senescence, cancer (Di Ruocco et al., 2018; Iskow et al., 2010; Luca et al., 2015; Rodić et al., 2014), and Alzheimer’s disease (Guo et al., 2018; Sun et al., 2018). These findings suggest that aging biology and transposon biology are tightly intertwined. However, whether TEs are drivers of aging and aging phenotypes or whether they are mere “innocent” bystanders of the aging process is still unknown.

In the human genome, the two most abundant families of TEs are the retrotransposons long interspersed element 1 (*LINE-1* or *L1*) and *Alu*. *Alu* transposons, in particular, have the largest number of copies, with ~1.1 million loci occupying ~9-11% of the genome (Lander et al., 2001; Venter et al., 2001). These retrotransposons are short (~300 base pairs) and require the *LINE-1* machinery for their own mobilization (Dewannieux et al., 2003; Rubin et al., 1980; Wallace et al., 2008). Further, the *Alu* family can be segregated into three subfamilies depending on evolutionary age: *AluJ* is the oldest lineage and likely immobile in humans, *AluS* is the middle-aged lineage containing some mobile copies, and *AluY* is the youngest lineage with the most functionally intact copies (Bennett et al., 2008). Evolutionarily, *Alu* elements are believed to have originated from 7SL RNA (Rubin et al., 1980; Ullu and Tschudi, 1984) which plays important roles in (1) co-translationally directing proteins to the endoplasmic reticulum as part of the protein

71 secretory pathway (Nyathi et al., 2013; Walter and Blobel, 1982; Wild et al., 2002) and (2)
72 orchestrating a cellular response to thermal stress that involves transcription and translation arrest
73 (Bujisic et al., 2025). Its evolutionary history suggests that *Alu* may play important roles in
74 regulating proteostasis, although this has not been thoroughly evaluated, and the breadth of *Alu*-
75 regulated pathways remains unclearly defined.

76 Thus far, the effects of elevated *Alu* expression in a non-diseased and non-senescent
77 background are ill-defined, and whether *AluJb* overexpression is sufficient to recapitulate
78 senescence or aging phenotypes is an open question. To address these gaps, we generated a
79 multi-omic resource encompassing transcriptomic, proteomic, and secretomic profiles of "healthy"
80 human primary IMR-90 fibroblasts overexpressing an *AluJb* retrotransposon, an element which
81 naturally becomes transcriptionally upregulated in human primary aging fibroblasts. We
82 demonstrate that this overexpression induces widescale remodeling of the transcriptome, cellular
83 proteome, and secretome, and that this remodeling partially reflects remodeling observed during
84 aging and senescence. On both a molecular and functional level, we observe *AluJb*-induced
85 alterations in mitochondrial metabolic activity, cell proliferation, and proteostasis—all pathways
86 that become mis-regulated during aging. Our results suggest that *AluJb* overexpression is
87 sufficient to promote senescence and aging-associated molecular and functional changes, and,
88 therefore, *AluJb* may partially promote senescence or aging phenotypes when de-repressed
89 under physiological conditions with aging.

RESULTS

Aging upregulates repetitive elements, including *Alu* transposons, in primary human fibroblasts

To systematically characterize the effects of aging on the repetitive transcriptome, we leveraged publicly available mRNA-sequencing data for human aging primary fibroblasts (Fleischer et al., 2018) (**Figure 1A**). Though others have explored the relationship between aging and transposon expression in these samples (LaRocca et al., 2020; Pabis et al., 2024), we note that our sample selection criteria were more stringent. To minimize batch effects and isolate aging effects without confounding effects from development, the final sample set we utilized included 76 samples with the following characteristics: male and female adults were aged between 20 and 96 years old, adults were of Caucasian ethnicity, and all fibroblasts were derived from skin on the arm.

Differential gene expression analysis identified 395 repeat subfamilies that increased with age and 33 subfamilies that decreased with age at an FDR < 0.05 (**Figure 1B, Supplementary Table S1A**). These effects were not specific to any repeat class, as specific DNA transposons, long interspersed elements (LINEs), short interspersed elements (SINEs), and long terminal repeat (LTR) transposons changed with age (**Supplementary Table S1A**). Because SINEs are a relatively understudied class of transposons despite being one of the most abundant classes in the human genome, we chose to focus on one of its subfamilies and characterize it further. Though a few SINE subfamilies changed with age, we decided to concentrate on the *AluJb* subfamily of retrotransposons, whose total expression increased with age (FDR = 1.02E-2, **Figure 1C**). After quantifying expression levels at individual repeat loci and aggregating counts by genomic context [as previously done in (Bravo et al., 2024)] (**Supplementary Table S1B**), we observed that intergenic *AluJb* copies within 5 kilobases of a gene (FDR = 2.03E-5) and exon-overlapping copies (FDR = 7.52E-3) both increased with age (**Figure 1C**). These results reiterate that transposon control mechanisms become dysregulated with age, and *Alu* transposon expression becomes elevated with age. Moreover, these results leave open the possibility that *AluJb* may exert cellular aging-associated effects either through its own independent transcripts or by incorporating itself into the transcripts of hosting genes.

To identify candidate pathways that may become mis-regulated in response to elevated *AluJb* expression, we carried out differential gene expression analysis across total *AluJb* expression levels (**Supplementary Table S1C**) followed by gene set enrichment analysis (GSEA). Interestingly, top Gene Ontology (GO) Biological Process terms associated with

123 proteostasis, such as 'ribosome biogenesis', 'rRNA metabolic process', and 'rRNA processing',
124 were significantly downregulated (**Figure 1D, Supplementary Table S1D**). Other terms
125 associated with mitochondrial metabolism (like 'aerobic respiration' and 'electron transport chain')
126 and the cell cycle (like 'mitotic nuclear division' and 'cell cycle phase transition') were also
127 significantly downregulated. In contrast, top terms associated with the extracellular matrix, such
128 as 'homophilic cell adhesion via plasma membrane adhesion molecules', were significantly
129 upregulated. In parallel, top Reactome pathways associated with the cell cycle, such as 'cell cycle,
130 mitotic' and 'M phase', as well as pathways associated with proteostasis, such as 'translation',
131 were downregulated (**Figure 1E, Supplementary Table S1E**). Similar to the GO analysis,
132 extracellular matrix-related terms such as 'extracellular matrix organization' were significantly
133 upregulated. These results highlight recurrent correlations between *AluJb* expression and
134 alterations in aging-associated pathways related to proteostasis, mitochondrial function, the cell
135 cycle, and the extracellular environment, and raise the intriguing possibility that *AluJb* expression
136 itself may drive these phenotypes.

137

138 ### *AluJb* promotes widespread transcriptional and proteomic remodeling

139 Our analysis identified numerous pathways correlated with *AluJb* expression levels in
140 aging fibroblasts, though it was unclear whether *AluJb* was an upstream driver of changes in
141 these pathways or whether it was a simple bystander. To begin to answer this question and
142 characterize the effects of elevated *AluJb* expression on primary cell phenotypes, we placed the
143 consensus sequence under the control of the U6 RNA polymerase III promoter and transiently
144 transfected human IMR-90 fibroblasts (**Figure 2A**). After a ~24 hours recovery period following
145 electroporation, cells were re-seeded at equal densities and cultured in low serum media in
146 accordance with previously described guidelines for generating conditioned media from
147 senescent cells and quiescent control cells (Neri et al., 2021). We implemented this protocol
148 because (1) we hypothesized that *Alu* overexpression may induce senescence-associated
149 changes and (2) this protocol utilizes serum deprivation to induce quiescence in order to isolate
150 senescent versus non-senescent effects and eliminate non-proliferating vs proliferating effects.
151 After 72 hours, cells and conditioned media were collected for transcriptomic, proteomic, and
152 secretomic analysis (**Figure 2A, Supplementary Tables S2A-C**). Importantly, overexpression of
153 plasmid-specific *AluJb* was verified by reverse transcription (RT) followed by endpoint polymerase
154 chain reaction (PCR) (**Figure S1A**).

155 Interestingly, multidimensional scaling (MDS) analysis segregated the empty vector
156 control cells from the *AluJb*-overexpressing cells across the transcriptome (**Figure 2B**), cellular
157 proteome (**Figure 2C**), and secretome (**Figure 2D**). This suggests that *AluJb* overexpression
158 induces major changes across "-omics" layers. Consistent with this notion, *AluJb* overexpression
159 induced a significant (FDR < 0.05) upregulation of 107 genes and a downregulation of 102 genes
160 (**Figure 2E, Supplementary Table S2D**), a significant (Q < 5% and abs($\log_2$FC) > 0.20)
161 upregulation of 62 cellular proteins and a downregulation of 57 cellular proteins (**Figure 2F,**
162 **Supplementary Table S2E**), and a significant (Q < 5% and abs($\log_2$FC) > 0.58) upregulation of
163 871 secreted proteins and a downregulation of 8 secreted proteins (**Figure 2G, Supplementary**
164 **Table S2F**). Additionally, though the segregation was not as strong as with the gene expression
165 profiles, the repeat subfamily expression profiles also segregated empty vector and *AluJb*-
166 overexpressing cells by MDS analysis (**Figure S1B**), highlighting major shifts in the repeat
167 transcriptome itself following *AluJb* overexpression. In line with this notion, we observed a trend
168 where *AluJb*-overexpressing cells had more reads mapping to repeat subfamilies compared to
169 control cells (**Figure S1C**). Moreover, the differential expression analysis identified 104 repeat
170 subfamilies with significantly (FDR < 0.05) higher expression and 1 repeat subfamily with
171 significantly lower expression in the overexpression group (**Figure S1D, Supplementary Table**
172 **S2D**). These repeat subfamilies belonged to several repeat classes, including DNA transposons,
173 LINEs, LTRs, and SINEs. Thus, these results suggest that elevated *AluJb* expression can
174 promote the de-repression of other repeats from diverse repeat classes, potentially forming
175 positive feedback loops where newly upregulated repeats further promote the expression of
176 additional repeats.

177 Importantly, to contextualize our results within the broader *Alu* research literature, we
178 compared our findings to a previous study of IMR-90 fibroblasts stably overexpressing two *AluS*
179 retrotransposons (Cantarella et al., 2019) (**Figure S2A**). We observed that genes upregulated by
180 *AluS* were significantly enriched among genes significantly upregulated by *AluJb* (Fisher's exact
181 p-value = 3.03E-3), and genes downregulated by *AluS* were significantly enriched among genes
182 significantly downregulated by *AluJb* (Fisher's exact p-value = 1.52E-6; **Figure S2B**). These
183 results demonstrate a degree of consistency between *AluS*- and *AluJb*-regulated genes. As an
184 alternative approach, we also generated gene sets for *AluS* induced and *AluS* repressed genes
185 and carried out gene set enrichment analysis (GSEA) among *AluJb*-driven transcriptomic
186 changes (**Figure S2C, Supplementary Table S2G**). Surprisingly, while the set of *AluS* induced
187 genes was consistently upregulated by *AluJb*, the set of *AluS* repressed genes was inconsistently
188 upregulated by *AluJb*. These results suggest that differences in the *Alu* subfamily (*AluJb* vs *AluS*)

189 or differences in the overexpression duration (transient vs stable) may induce partially unique
190 cellular responses and phenotypic effects.

191

192 ### *AluJb* overexpression elicits aging- and senescence-associated molecular alterations

193 Transposon de-repression is often seen in aging and in cellular senescence, but it is
194 unclear whether aging and senescence follow transposon de-repression, or whether TE de-
195 repression follows aging and senescence. To test the former idea, we compared our multi-omics
196 measurements to published lists of senescence-induced or aging-induced gene changes (**Figure**
197 **3A**). Since our experimental approach was originally designed to capture senescence-associated
198 secretory phenotype (SASP) factors (Neri et al., 2021), we first compared our multi-omics results
199 to a list of core SASP factors (Basisty et al., 2020). Indeed, core SASP factors were enriched (p
200 = 2.19E-2) among significant, rather than non-significant, differentially expressed genes (**Figure**
201 **3B**). Additionally, there was a suggestive enrichment of core SASP factors among significant,
202 rather than non-significant, differentially abundant cellular or secreted proteins (**Figure 3C-3D**).
203 These results suggest that *AluJb* may drive differences in core SASP factors across the
204 transcriptome, cell proteome, and secretome.

205 For heightened sensitivity and to determine the directionality of any observed changes,
206 we carried out gene set enrichment analysis (GSEA) with several aging and senescence gene
207 sets. At the transcriptomic level, we observed that (1) genes downregulated with age in the
208 Genotype-Tissue Expression (GTEx) project (Jia et al., 2018), (2) genes downregulated with age
209 in human primary fibroblasts (Fleischer et al., 2018), and (3) repetitive elements upregulated with
210 age in human primary fibroblasts significantly (FDR < 0.05) changed with the same directionality
211 following *AluJb* overexpression (**Figure 3E, Supplementary Table S3A**). Other gene sets like
212 Senmayo (Saul et al., 2022) and the core SASP were also significantly repressed following
213 overexpression, while repeats that were downregulated in human aging primary fibroblasts were
214 significantly upregulated following overexpression. At the cellular proteomics level, core SASP
215 factors were significantly (FDR < 0.05) upregulated following *AluJb* overexpression (**Figure 3F,**
216 **Supplementary Table S3B**). We observed that genes downregulated with age in the GTEx
217 project were significantly upregulated at the protein level following overexpression, but the
218 directionality was inconsistent. Finally, at the secretomics level, core SASP factors were
219 significantly (FDR < 0.05) upregulated following *AluJb* overexpression (**Figure 3G,**
220 **Supplementary Table S3C**). These factors included insulin-like growth factor binding proteins
221 (like IGFBP4 and IGFBP5), matrix metalloproteinases (like MMP1 and MMP2), and tissue

222 inhibitors of metallopeptidase (like TIMP1). Though some of the effects vary in directionality, these
223 results suggest that elevated *AluJb* expression can partially mirror molecular changes observed
224 during cellular senescence and aging. Additionally, the significant upregulation of core SASP
225 factors in the secretome highlights *AluJb* as a potential driver of inflammation and altered
226 intercellular communication.

227 We next tested the inverse hypothesis that transposon-mediated effects would follow
228 chronological aging (**Figure S3A**). Surprisingly, *AluJb*-induced genes were not significantly
229 enriched among significant primary fibroblast aging genes, and downregulated *AluJb* genes were
230 actually significantly depleted compared to their frequency among nonsignificant aging
231 downregulated genes (**Figure S3B**). GSEA highlighted an inverted regulation of *AluJb*-induced
232 genes with aging, where *AluJb* downregulated genes were upregulated with age and *AluJb*
233 upregulated genes were downregulated with age (**Figure S3C, Supplementary Table S3D**). In
234 contrast, many repetitive elements that were upregulated following *AluJb* overexpression were
235 also upregulated in aged primary human fibroblasts (**Figure S3D-S3E, Supplementary Table**
236 **S3D**). These results demonstrate that aging partially recapitulates the effects of *AluJb* and the
237 upregulation of many endogenous repetitive elements, in particular. Taken together with the
238 observation that *AluJb* is sufficient to induce aging- and senescence-associated changes, these
239 results suggest the existence of a complex feedback mechanism whereby (1) *AluJb* can promote
240 aging and senescence, (2) aging can promote heightened repetitive element expression, creating
241 feedback loop pressure, and (3) aging simultaneously regulates *AluJb*-induced gene expression.

242

243 *AluJb* drives molecular changes in mitochondrial, proteostasis, cell cycle, and 244 extracellular matrix pathways

245 To assign functions to molecular changes caused by elevated *AluJb* expression, we
246 carried out gene set enrichment analysis (GSEA) in each individual "-omics" layer using functional
247 gene set collections (**Figure 4A**). In the transcriptome and using the Gene Ontology (GO)
248 Biological Process gene set collection, we identified an upregulation of extracellular matrix-related
249 processes (*e.g.* "homophilic cell adhesion via plasma membrane adhesion molecules" and "cell
250 junction organization"), as well as cell cycle-related processes (*e.g.* 'regulation of mitotic sister
251 chromatid segregation'; **Figure 4B, Supplementary Table S4A**). We also observed a
252 downregulation of terms related to mitochondrial metabolism (*e.g.* "aerobic respiration" and
253 "generation of precursor metabolites and energy") and proteostasis (*e.g.* "cytoplasmic
254 translation"). In the cellular proteome, the top upregulated processes were related to the cell cycle

255 (*e.g*. “cell cycle G2/M phase transition”) and to protein phosphorylation (*e.g*. “regulation of
256 dephosphorylation”; **Figure 4C, Supplementary Table S4B**). Finally, in the secretome, the top
257 upregulated terms were related to responding to stimuli (*e.g*. “response to endogenous stimuli”
258 and “response to transforming growth factor beta”) and the top downregulated terms were related
259 to aspects of proteostasis (*e.g*. “rRNA processing”; **Figure 4D, Supplementary Table S4C**).
260 GSEA with Reactome pathway gene sets (Milacic et al., 2023) mirror many of the results obtained
261 using the GO Biological Process terms. In the transcriptome, we again observed an upregulation
262 of extracellular matrix-related pathways (*e.g*. “extracellular matrix organization” and “integrin cell
263 surface interactions”) and a downregulation of proteostasis pathways (*e.g*. “eukaryotic translation
264 elongation” and “eukaryotic translation termination”) and mitochondrial metabolic pathways (*e.g*.
265 “aerobic respiration and respiratory electron transport”; **Figure 4E, Supplementary Table S4D**).
266 In this case, we could not detect significantly (FDR < 0.05) altered pathways in the cellular
267 proteome (**Figure 4F**). However, the secretome also exhibited an upregulation of extracellular
268 matrix-associated pathways, as well as a downregulation of pathways related to DNA repair or
269 epigenetic modifications (*e.g*. “base-excision repair, AP site formation” and “chromatin
270 modifications during the maternal to zygotic transition”; **Figure 4G, Supplementary Table S4E**).
271 These results demonstrate that *AluJb* can regulate functional pathways that are often differentially
272 regulated with age.

273 To ensure that these pathway-level changes were not unique to serum deprived cells and
274 were also observed in proliferating cells (where more of these pathways could be functionally
275 tested without the added stress of serum-deprivation), we carried out an additional transcriptomic
276 analysis of proliferating IMR-90 fibroblasts cultured in standard rich media (**Figure S4A**). Again,
277 we confirmed plasmid-specific *AluJb* overexpression by PCR (**Figure S4B**), observed a
278 segregation of control and overexpression samples by MDS analysis of gene (**Figure S4C**) and
279 repeat (**Figure S4D**) expression profiles, and observed a trending increasing in the percent of
280 reads mapping to repeat subfamilies following *AluJb* overexpression (**Figure S4E**). We observed
281 a significant (FDR < 0.05) increase in 3790 genes and a decrease in 987 genes, as well as an
282 increase in 201 repeat subfamilies (**Figure S4F, Supplementary Table S4F**). The altered repeat
283 subfamilies belonged to several repeat classes, including DNA transposons, LINEs, and LTRs.
284 GSEA analysis with GO Biological Process gene sets highlighted an upregulation of cell cycle
285 processes (*e.g*. “chromosome segregation” and “centriole assembly”) and a repression of
286 mitochondrial metabolic processes (*e.g*. “aerobic respiration” and “oxidative phosphorylation”)
287 and proteostasis processes (*e.g*. “protein folding”) (**Figure S4G, Supplementary Table S4G**).
288 Likewise, GSEA with Reactome pathway gene sets highlighted a repression of proteostasis

289 pathways (*e.g*. “eukaryotic translation elongation”, “peptide chain elongation”, and “HSF1
290 activation”) and mitochondrial metabolic pathways (**Figure S4H, Supplementary Table S4H**).
291 These results demonstrate that *AluJb* can also promote broad molecular alterations in rich media
292 conducive to cell proliferation.

293 Using the initial transcriptomic data, we next sought to characterize *AluJb*-induced
294 alterations across broad gene modules (**Figure 5A**). An enrichment analysis of transcription factor
295 (TF) regulons identified heat shock transcription factor 1 (HSF1) as one of the top TFs with
296 repressed targets (**Figure 5B, Supplementary Table S4I**). Since HSF1 plays a crucial role in the
297 heat shock response and therefore in maintaining proteostasis during stress (Pincus, 2020), these
298 results highlight potential master regulators of the previously noted *AluJb*-driven pathway
299 alterations. Indeed, PRRX1 has been identified as a master transcription factor in stromal
300 fibroblasts with functions related to extracellular remodeling (Lee et al., 2022), ETV5 regulates
301 fatty acid metabolism through peroxisome proliferator-activated receptor (PPAR) signaling (Mao
302 et al., 2021), and both KDM5A and CXXC1 play roles in epigenetic control (Blair et al., 2011;
303 Kiuchi et al., 2021). Additionally, a network analysis to construct a predicted protein-protein
304 interaction (PPI) network using significantly differentially expressed genes highlighted two major
305 clusters of corresponding proteins: one with proteins involved in mitochondrial function, such as
306 *MT-ND2, MT-ND4, MT-ND5,* and *MT-ND6*, and one with proteins involved in translation, such as
307 *RPS25* and *RPL36AL* (**Figure 5C**). These results further highlight broad-scale *AluJb*-driven
308 alterations in molecular pathways involved with the extracellular environment, epigenetics,
309 metabolism, and proteostasis.

310

311 **Multi-omic integration highlights alterations in extracellular, proteostasis, and metabolic**
312 **pathways**

313 To further increase sensitivity and identify pathways alterations occurring in more than
314 one “-omics” analysis, we carried out multi-contrast gene set enrichment analysis (**Figure 6A**).
315 Indeed, an overlap analysis of individual significant genes/proteins across “-omics” analyses was
316 limited, and we identified four genes and corresponding proteins—*DCN, NES, POSTN*, and *DBI*—
317 that changed in all three “-omics” layers (**Figure 6B**, **Figure S5A-S5C**). This modest overlap could
318 result from multiple technical and biological reasons, including different detection sensitivities
319 across “-omics” layers and imperfect correlations between “-omics” layers. In these cases,
320 combinatorial analyses taking into account multiple “-omics” layers *a priori* (in the process of

321 enrichment analysis) instead of *a posteriori* (overlapping differential results in each independent
322 dataset) are more powerful to detect consistent functional changes elicited across layers.

323 Thus, we performed multi-contrast gene set enrichment analysis using a rank MANOVA
324 framework to identify pathways consistently regulated across our multi-omics profiling (**Figure 6**).
325 We first leveraged GO Biological Process terms, which revealed that the transcriptome was most
326 similar to the secretome, and that the cell proteome varied compared to the other two "-omics"
327 types (**Figure 6C, Supplementary Table S5A**). This analysis also identified extracellular matrix-
328 related terms, such as 'external encapsulating structure organization', 'cell adhesion', and 'cell
329 motility', that were upregulated across the transcriptome and secretome but varied in the cell
330 proteome (**Figure 6C-6D**). Similarly, proteostasis terms like 'cytoplasmic translation' and
331 'ribosomal small subunit biogenesis' were suppressed in the transcriptome and secretome but
332 varied in the cell proteome (**Figure 6C-6D**). The multi-contrast analysis with the Reactome
333 pathway gene sets also highlighted a stronger similarity between the transcriptome and
334 secretome compared to the cell proteome (**Figure 6E, Supplementary Table S5B**). Mirroring the
335 previous analysis, extracellular matrix terms like 'extracellular matrix organization' and
336 'degradation of the extracellular matrix' were upregulated across the three "-omics" analyses,
337 while proteostasis terms like 'cap-dependent translation initiation' and 'SRP-dependent
338 cotranslational protein targeting to membrane' were downregulated across all three "-omics"
339 layers (**Figure 6E-6F**). These results further emphasize widespread alterations that are
340 consistently observed in more than one "-omics" layer following *AluJb* overexpression.

341

342 ## *AluJb* overexpression leads to functional alterations, as predicted from multi-omics
343 alterations

344 Our individual and integrated multi-omics analyses identified molecular changes
345 associated with several aging-regulated functional pathways, including mitochondrial metabolism,
346 the cell cycle, and proteostasis, among others. However, whether these molecular changes
347 translated to functional cellular changes remained unclear. To test the functional effects of *AluJb*
348 on cell physiology, we thus carried out several functional assays (**Figure 7A**).

349 First, we assessed mitochondrial respiration using a Seahorse Cell Mito Stress Test
350 (**Figure 7B**). This revealed a significant ($p < 0.05$) reduction in many oxygen consumption rate
351 (OCR)-related metrics, including basal respiration, maximal respiration, non-mitochondrial
352 respiration, ATP-linked respiration, proton leak, and spare capacity (**Figure 7B**, **Figure S6A-**

353 **S6B**). Though this assay is not specifically designed to evaluate resting glycolytic rate, parallel
354 measurements of extracellular acidification rate did not reveal any significant differences in resting
355 glycolytic rate (**Figure 7C**). These results demonstrate that mitochondrial respiration (but likely
356 not glycolytic potential) is substantially dampened following *AluJb* overexpression, consistent with
357 aging.

358 Next, we carried out a propidium iodide-based cell cycle assay (**Figure 7D, Figure S6C**).
359 Since cell proliferation is one of a limited number of phenotypes known to be disrupted by *Alu*
360 expression (Cantarella et al., 2019), we chose to re-analyze this phenotype since it (1) appeared
361 in our analyses and (2) could serve as a potential positive control. Though we did not detect
362 significant differences between control and *AluJb*-overexpressing cells in the G0/G1 and G2/M
363 phases, we did detect a significant ($p < 0.05$) accumulation of *AluJb*-overexpressing cells in the
364 S phase, consistent with a prior report (Cantarella et al., 2019). However, contrary to this report,
365 we interpret this accumulation in S-phase to represent likely replication stress rather than
366 increased proliferative potential (based on total cell numbers over the course of our experiment,
367 as well as the lack of a concomitant increase in G2/M cells). These results demonstrate a buildup
368 of cells in the S phase, which may be caused by replication stress or stalling.

369 Finally, since we detected alterations in proteostasis-related pathways, we carried out a
370 Proteostat Aggresome detection assay to identify differences in protein aggregate buildup (**Figure**
371 **7E, Figure S6D**). Interestingly, we observed a significantly ($p < 0.05$) lower median fluorescence
372 intensity in the *AluJb*-overexpressing cells compared to control cells. These results demonstrate
373 a reduced buildup of protein aggregates and further highlight alterations in proteostasis
374 machinery.

375 Taken together, our molecular multi-omics analyses combined with functional profiling
376 reveal *AluJb* retrotransposon-induced changes in several of the hallmarks of aging (**Figure 7F**)
377 (Kroemer et al., 2025). These include changes associated to (1) primary hallmarks like loss of
378 proteostasis, epigenetic alterations, and genomic instability, (2) antagonistic hallmarks like
379 mitochondrial dysfunction, and (3) integrative hallmarks like extracellular matrix changes, altered
380 intercellular communication, and cell cycle changes that can manifest as stem cell exhaustion.
381 Our results suggest that elevated *AluJb* retrotransposon expression is sufficient to drive mis-
382 regulation of aging-related pathways, and may thus directly contribute to aging phenotypes.

383

384 ## DISCUSSION

385 ### *A new resource for studying the effects of increased transposon expression*

386 In this study, we generated a multi-faceted resource for studying the effects of elevated
387 *AluJb* transposon expression in "healthy" human IMR-90 fibroblasts. This resource encompasses
388 a multi-omics characterization of the transcriptome, cell proteome, and secretome for human
389 fibroblasts with and without *AluJb* overexpression. This resource expands the limited number of
390 "-omics" resources where TE expression was directly modulated, including the previously
391 mentioned transcriptomic study with stable *AluS* overexpression in IMR-90 fibroblasts (Cantarella
392 et al., 2019), and a transcriptomic study with stably-integrated but inducible codon-optimized
393 *LINE-1* expression in immortalized retinal pigment epithelial (RPE) cells (Ardeljan et al., 2020).
394 Because RNA and protein levels do not always correlate (Vogel and Marcotte, 2012), our study
395 addresses molecular blind-spots present in prior studies focusing on a single "-omics" layer.
396 Importantly, because aging involves the deterioration of healthy organs, tissues, and cells, it will
397 be important (1) to identify and characterize the regulatory mechanisms that fail with age in
398 healthy organs, tissues, and cells, especially those that relate to transposon control, and (2) to
399 characterize the effects of elevated transposon expression in healthy organs, tissues, and cells.
400 In contrast to other studies utilizing cancer or immortalized cell lines to study transposons, our
401 resource is primed for studying the causes and consequences of elevated transposon expression
402 in "healthy", non-cancerous, and non-immortalized cells. By integrating this resource with existing
403 and newly-generated "-omics" resources where transposon expression is experimentally
404 manipulated, it will be possible to characterize (1) organ-, tissue-, and cell type-specific changes
405 in response to transposon expression, as well as (2) common and unique responses to different
406 transposon families, subfamilies, or loci. Ultimately, we anticipate that this resource will be a
407 useful starting point for answering these questions, especially as they relate to senescence and
408 aging.

409 Our study also provides molecular signatures for elevated *AluJb* expression that can be
410 readily incorporated into ongoing senescence, aging, therapeutic, or other studies with an interest
411 in transposon control. Like the aging and senescence gene sets used to determine whether aging
412 or senescence may be regulated by *AluJb*, the *AluJb* gene sets and protein sets we present can
413 be used to determine whether transposon activation may be regulated by aging, senescence, or
414 any other treatment of interest. As elevated transposon activity is a feature of many aging-
415 associated diseases like cancer (Di Ruocco et al., 2018; Iskow et al., 2010; Luca et al., 2015;
416 Rodić et al., 2014) and Alzheimer's disease (Guo et al., 2018; Sun et al., 2018), our molecular

417 signatures can be used to simultaneously determine the effects of the disease and the effects of
418 candidate therapeutics on transposon activity. Thus, we believe this resource holds promising
419 potential for more thoroughly characterizing human diseases and the therapeutics used to treat
420 them.

421

422 ***Transposons as drivers of senescence and aging***

423 This study presents several observations that are consistent with the hypothesis that *AluJb*
424 retrotransposons partially drive senescence and aging. First, we find that *AluJb* retrotransposons
425 are upregulated in human aging primary fibroblasts, and their expression is correlated with
426 alterations in pathways related to the hallmarks of aging (Kroemer et al., 2025), including
427 pathways involved in mitochondrial metabolism, proteostasis, the cell cycle, and the extracellular
428 matrix. Second, we find that *AluJb*-induced transcriptomic changes partially mirror transcriptomic
429 changes in human aging primary fibroblasts and in the GTEx project. Moreover, both the cell
430 proteome and secretome exhibited a significant upregulation of core SASP factors. Third, we find
431 that functional pathways responding to *AluJb* overexpression are also related to the hallmarks of
432 aging and include the pathways mentioned in the first point. Finally, we find that *AluJb*
433 overexpression promotes differences in cell functions related to the hallmarks of aging. Our
434 results add to the growing litany of studies demonstrating that *Alu* retrotransposons promote
435 features of aging.

436 Though the effects of *Alu* on cell function have not been broadly, unbiasedly, and
437 extensively studied with "-omics" approaches, several targeted studies have explored *Alu*'s
438 relationship to specific aging-regulated pathways, such as mitochondrial metabolism and the cell
439 cycle. *Alu*'s influence on mitochondrial function has been explored in the context of advanced
440 age-related macular degeneration. Specifically, in human cell culture and mouse models, *Alu*
441 RNA was sufficient to promote opening of the mitochondrial permeability transition pore, release
442 of mtDNA into the cytosol, and activation of inflammatory cGAS-STING signaling (Kerur et al.,
443 2017). Whether this mechanism is specific to advanced age-related macular degeneration or is
444 more broadly applicable to other aging contexts is an open question. Nonetheless, the
445 mitochondrial dysfunction observed in that study is consistent with the repression of mitochondrial
446 metabolism observed in this study.

447 With respect to cell cycle alterations, at least three studies have explored their relationship
448 to *Alu* RNA levels. First, *Alu* transcripts were found necessary for senescence, as knockdown of

449 *Alu* transcripts promoted exit of adult adipose-derived mesenchymal stem cells from senescence
450 (Wang et al., 2011). Second, consistent with this senescence-promoting model, introducing *Alu*
451 RNA into RPE cells from humans with advanced age-related macular degeneration led to the
452 upregulation of pro-inflammatory and senescence markers, including *IL-18, IL-1β, p16*^{INK4a}, and
453 SPiDER-βGal staining (Yamada et al., 2020). Third, stable overexpression of two *AluS* elements
454 in IMR-90 human fibroblasts was shown to upregulate cell cycle genes and induce an
455 accumulation of cells in the S phase (Cantarella et al., 2019). Though the authors speculated that
456 the S phase accumulation reflects heightened cell proliferation, an alternative, more likely
457 hypothesis is that it represents replication stress or stalling. Indeed, similar to this study, we also
458 observe an accumulation of cells in the S phase without a concurrent accumulation in the G2/M
459 phase, supporting the notion of replication stalling. Moreover, though we don't detect a significant
460 enrichment of senescence gene sets in any "-omics" layers, we do observe a significant
461 upregulation of core SASP factors.

462 Taken together, our study, combined with previously published studies, highlight the
463 possibility that transcriptional upregulation of *Alu* transposons is sufficient to promote features of
464 cellular senescence or aging.

465

466 ***Limitations of the study***

467 While we believe that physiologically-relevant principles about *Alu* biology can be readily
468 extracted from this study, we note potential further considerations. First, there are several viable
469 options to choose from concerning any specific transposon to modulate, even when restricting
470 the choice to a specific family, like *Alu*. We chose to focus on an *AluJb* element, instead of an
471 *AluS* or *AluY* element, because (1) we observed that *AluJb* increased with age in human primary
472 fibroblasts, making it a suitable candidate for studying its potential age-related effects and (2) we
473 hypothesized that mobilization of an *AluJ* element would be much more restricted compared to
474 an *AluS* or *AluY* element, potentially allowing us to focus on the effects of its transcriptional
475 upregulation with minimal or reduced effects from mobilization. Additionally, we chose to use a
476 consensus *AluJb* sequence instead of the sequence of a specific *AluJb* copy. We believe that the
477 former approach can provide more generalizable results across *Alu* copies, and the latter
478 approach would be better suited for identifying transposon locus-specific effects. Since we were
479 interested in broad and conserved effects, we opted for the consensus sequence option.

Secondly, there are several options concerning the gene expression manipulation paradigm. We opted for a transient overexpression of *AluJb*, though stable *Alu* overexpression lines have been previously generated (Cantarella et al., 2019). A comparison of the results from these two approaches suggests that they at least partially mirror each other (**Figure S2**). However, depending on whether one is interested in characterizing the effects of transient versus sustained *AluJb* expression, one approach may be better suited for the research question at hand. Although a stable overexpression approach may better model the sustained transposon expression observed during aging, "healthy" cells may have time to respond to the overexpression and employ compensatory regulatory mechanisms, such as DNA methylation, to restrict its impact. In addition, genetic drift occurring during selection may add noise to the analysis. This may or may not change the utility of the approach in modeling transposon-aging interactions. In the future, overexpression approaches could be complemented by the incorporation of knockdown approaches which can target endogenous *Alu* expression to provide additional insights.

Finally, there are several options concerning the demographics underlying the samples being considered for experimentation. In this proof-of-principle study, we utilized a well-characterized female primary embryonic fibroblast cell line, IMR-90. As aging phenotypes, including TE expression, are frequently sex-dimorphic (Sampathkumar et al., 2020), it would be important to characterize both the common and sex-specific effects of *AluJb* overexpression, especially as they relate to aging. Additionally, though we used IMR-90 embryonic fibroblasts because of their frequent use as a model for studying senescence and aging, it would also be informative to assess the effects of *Alu* overexpression in adult primary fibroblasts, which may provide a more physiological environment to model the effects of elevated *Alu* expression with age. Ultimately, we believe this study serves as a useful starting point – a proof-of-principle - for the characterization of the relationship between transposon expression and aging.

RESOURCE AVAILABILITY

Lead contact

Further information and requests for resources and reagents should be directed to and will be fulfilled by the lead contact, Bérénice A. Benayoun (bbenayou@usc.edu).

Materials availability

The plasmids generated in this study, pUC19-U6 (ID: 240313) and pUC19-U6_AluJb (ID: 240314), are available through Addgene.

Data and code availability

- RNA-seq data have been deposited at the Sequence Read Archive (SRA) under BioProject PRJNA1008694.
- Raw data and complete mass spectrometry data sets have been uploaded to the Mass Spectrometry Interactive Virtual Environment (MassIVE) repository, developed by the Center for Computational Mass Spectrometry at the University of California San Diego, and can be downloaded using the following link: https://massive.ucsd.edu/ProteoSAFe/dataset.jsp?task=42e058c0f1244315aa9d3e61add4cdd3 (MassIVE ID number: MSV000097822; ProteomeXchange ID: PXD063739).
- Original DNA gel images, raw Agilent Seahorse data, and raw flow cytometry data have been deposited at Figshare at [DOI: 10.6084/m9.figshare.28928147].
- All scripts used to analyze the data in this manuscript are available on the Benayoun Lab GitHub at [https://github.com/BenayounLaboratory/AluJB_fibroblast_overexpression].
- Any additional information required to reanalyze the data reported in this paper is available from the lead contact upon request.

ACKNOWLEDGMENTS

This material is based upon work supported by the National Science Foundation Graduate Research Fellowship Program (NSF GRFP) under Grant No. DGE-1842487 (to J.I.B.), the National Institute on Aging (NIA) under Grant No. T32 AG052374 (to J.I.B.), the University of Southern California with a Provost Fellowship (to J.I.B.), and the National Institute of General Medical Sciences (NIGMS) under Grant No. R35 GM142395 (to B.A.B). This work was also made

possible by a pilot award under NIA grant P30 AG068345 (USC-Buck Institute Nathan Shock Center of Excellence) and by the NIH-OD instrumentation grant S10 OD028654 (to B.S.) for the Orbitrap Eclipse Tribrid mass spectrometry system.

We would like to thank Hemal Mehta at the USC Leonard Davis School of Gerontology Seahorse Core for conducting the seahorse assays. We are saddened by the passing of Dr. Judith Campisi and gratefully acknowledge her valuable contribution to this work.

Some artwork was taken from NIAID NIH BIOART Source (bioart.niaid.nih.gov) or from Bioicons (bioicons.com).

AUTHOR CONTRIBUTIONS

Juan I. Bravo: Conceptualization, Data curation, Investigation, Formal analysis, Visualization, Writing – original draft (co-lead), Writing – review & editing. **Eyael Tewelde:** Investigation, Formal analysis, Writing – review & editing (co-lead). **Christina D. King:** Investigation, Formal analysis, Writing – original draft, Writing – review & editing. **Joanna Bons:** Investigation, Formal analysis, Writing – original draft, Writing – review & editing. **Samah Shah:** Investigation, Writing – review & editing. **Jacob Rose:** Investigation, Writing – review & editing. **Judith Campisi:** Conceptualization. **Birgit Schilling:** Conceptualization, Formal analysis, Writing – original draft, Writing – review & editing, Supervision, Funding acquisition. **Bérénice A. Benayoun:** Conceptualization, Data curation, Formal analysis, Visualization, Writing – original draft (co-lead), Writing – review & editing (co-lead), Supervision, Funding acquisition.

DECLARATION OF INTERESTS

The authors declare that they have no competing interests. The content is solely the responsibility of the authors and does not necessarily represent the official views of the National Institutes of Health.

SUPPLEMENTAL INFORMATION

Document S1. Supplementary Figures S1–S6 and Supplementary Tables S1-S5

568 FIGURE TITLES AND LEGENDS

569 **Figure 1. Aging upregulates repetitive elements, including *Alu* transposons, in primary**
570 **human fibroblasts.**

571 **(A)** A diagram illustrating the transcriptomic time course analysis carried out using a publicly-
572 available mRNA-sequencing dataset (GSE113957) for N = 76 aging primary human fibroblasts.
573 **(B)** Gene expression heatmap for significant (FDR < 0.05) differentially expressed repeat
574 subfamilies across age. **(C)** Scatterplots for the library size-normalized counts across age for the
575 total *AluJb* subfamily expression, the *AluJb* subfamily expression from intergenic loci within 5
576 kilobases from a gene, and the *AluJb* subfamily expression from loci overlapping gene exons. All
577 three differential expression results were significant at an FDR < 0.05. Differential gene
578 expression analysis across total endogenous *AluJb* expression was carried out, followed by gene
579 set enrichment analysis, and the top 5 significant (FDR < 0.05) **(D)** GO Biological Process and
580 **(E)** Reactome pathway gene sets were plotted. FDR: False Discovery Rate.

581

582 **Figure 2. *AluJb* promotes widespread transcriptional and proteomic remodeling.**

583 **(A)** A diagram illustrating how control and *AluJb* overexpressing IMR-90 fibroblast samples were
584 prepared for multi-omic profiling. N = 5 replicates were independently transfected per group, and
585 N = 4 replicates were analyzed by mRNA-sequencing, N = 5 replicates were analyzed by cellular
586 proteomic profiling, and N = 4 replicates were analyzed by secretome profiling. Multidimensional
587 scaling (MDS) analysis of the **(B)** genic transcriptome, **(C)** cellular proteome, and **(D)** secretome.
588 Abundance heatmaps for significant **(E)** differentially expressed genes (FDR < 0.05), **(F)**
589 differentially abundant cellular proteins (Q < 5% and abs($\log_2$FC) > 0.20), and **(G)** differentially
590 secreted proteins (Q < 5% and abs($\log_2$FC) > 0.58). FDR: False Discovery Rate, Q: Q-value. See
591 also Figure S1 and S2.

592

593 **Figure 3. *AluJb* overexpression elicits aging- and senescence-associated molecular**
594 **alterations.**

595 **(A)** A diagram illustrating how *AluJb*-induced multi-omic changes and either senescence- or
596 aging-induced features were compared. Mosaic plots showing the fraction of core SASP factors
597 found among significant and non-significant *AluJb*-induced **(B)** mRNAs, **(C)** cellular proteins, and
598 **(D)** secreted proteins. Statistical significance of frequency differences was assessed with Fisher's
599 exact test, and p < 0.05 was considered significant. GSEA analysis with gene sets for

600 senescence- and aging-induced features in the *AluJb* **(E)** transcriptome, **(F)** cellular proteome,
601 and **(G)** secretome. Gene sets with FDR < 0.05 were considered significant. SASP: Senescence-
602 Associated Secretory Phenotype, FDR: False Discovery Rate, NES: Normalized Enrichment
603 Score. See also Figure S3.

604

605 **Figure 4. *AluJb* drives molecular changes in mitochondrial, proteostasis, cell cycle, and**
606 **extracellular matrix pathways.**
607 **(A)** A diagram illustrating how functional annotations were assigned to transcriptomic and
608 proteomic changes with gene set enrichment analysis. The top 5 significant (FDR < 0.05) GO
609 Biological Process gene sets in the **(B)** transcriptome, **(C)** cellular proteome, and **(D)** secretome
610 were plotted. The top 5 significant (FDR < 0.05) Reactome pathway gene sets in the **(E)**
611 transcriptome, **(F)** cellular proteome, and **(G)** secretome were also plotted. FDR: False Discovery
612 Rate, NES: Normalized Enrichment Score. See also Figure S4.

613

614 **Figure 5. *AluJb* overexpression leads to disruption of transcription factor regulons and**
615 **predicted PPI networks.**
616 **(A)** A diagram illustrating how the effects of *AluJb* on IMR-90 transcriptional networks was
617 assessed. **(B)** Significantly ($p < 0.05$) enriched or depleted transcription factor regulons were
618 identified with decoupleR, and the top 5 by magnitude were plotted. **(C)** Significant (FDR < 0.05)
619 differentially expressed genes were used to construct a combined protein-protein interaction (PPI)
620 and signaling network with NetworkAnalyst. The most populated subnetwork is shown. Blue
621 nodes represent downregulated genes, and red nodes represent upregulated genes. FDR: False
622 Discovery Rate.

623

624 **Figure 6. Multi-omic integration highlights alterations in extracellular, proteostasis, and**
625 **metabolic pathways.**
626 **(A)** A diagram illustrating how transcriptome, proteome, and secretome changes were integrated
627 via multi-contrast gene set enrichment analysis. **(B)** Venn diagram comparing individual genes
628 and proteins that significantly changed in each "-omics" analysis. Highlighted are four genes and
629 corresponding protein products—*DCN, NES, POSTN*, and *DBI*—that were altered in all three "-
630 omics" layers. The top 25 multi-contrast gene set enrichment results using **(C)** GO Biological

631 Process and **(E)** Reactome pathway gene sets. Gene sets with an adjusted MANOVA p-value <
632 0.05 were considered significant. Violin plots for select **(D)** GO Biological Process and **(F)**
633 Reactome pathway gene sets related to recurring pathway themes are shown. See also Figure
634 S5.

635

636 **Figure 7. *AluJb*-induced functional alterations mirror molecular alterations and are**
637 **consistent with disruption of aging hallmarks.**
638 **(A)** A diagram illustrating how the functional effects of *AluJb* overexpression were assessed. **(B)**
639 A representative oxygen consumption rate time course from one experiment with N = 6 per group.
640 Points represent means at each timepoint, and error bars represent the standard error of the
641 mean. Two experiments, with a total of N = 12 per group, were used to calculate several OCR
642 sub-metrics, including basal OCR and maximal OCR. Statistical significance was assessed with
643 a Wilcoxon rank sum test, and $p < 0.05$ was considered significant. **(C)** A representative
644 extracellular acidification rate time course from one of the aforementioned experiments. Points
645 represent means at each timepoint, and error bars represent the standard error of the mean. Both
646 experiments were used to calculate the resting ECAR, and statistical significance was assessed
647 with a Wilcoxon rank sum test. **(D)** Representative flow cytometry histograms for propidium iodide-
648 stained control and *AluJb* overexpressing cells. Three experiments were combined, for a total of
649 N = 18 per group, and the relative number of cells in G0/G1, S, and G2/M phases in the control
650 and overexpression group were compared with a Wilcoxon rank sum test. $p < 0.05$ was
651 considered significant. **(E)** Representative flow cytometry histograms for Proteostat-stained
652 control and *AluJb* overexpressing cells. Four experiments were combined, for a total of N = 24
653 per group, and the relative median fluorescence intensities between the control and
654 overexpression groups were compared with a Wilcoxon rank sum test. $p < 0.05$ was considered
655 significant. **(F)** A diagram summarizing the findings from this study as they relate to the hallmarks
656 of aging. OCR: Oxygen Consumption Rate, ECAR: Extracellular Acidification Rate, MFI: Median
657 Fluorescence Intensity. See also Figure S6.

Figure 1

A Scheme for assessing age-related transcriptomic changes in fibroblasts

Obtain transcriptomic data for aging human primary fibroblasts (GSE113957)

Gene expression time course analysis using DESeq2

B Significant (FDR 5%) differentially expressed repeat subfamilies across age

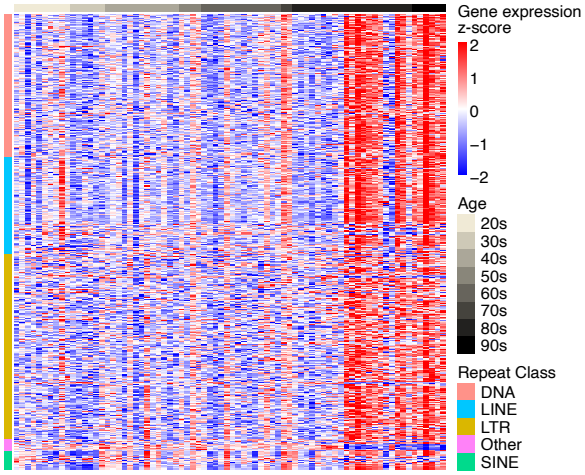

395 increase and 33 decrease

C AluJb subfamily expression across age

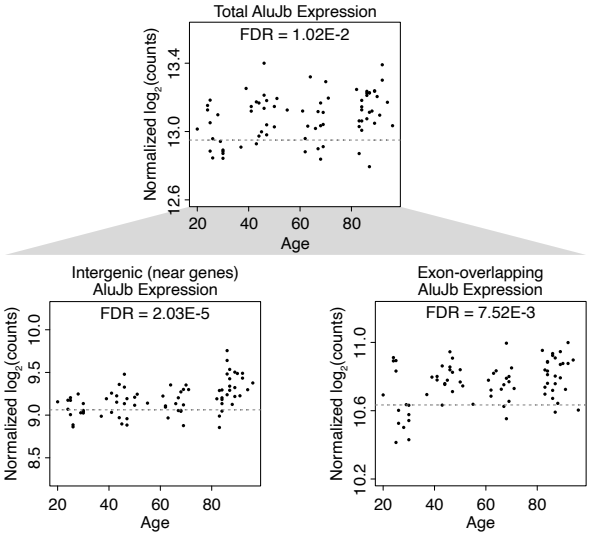

D GSEA across AluJb expression using GO Biological Process terms

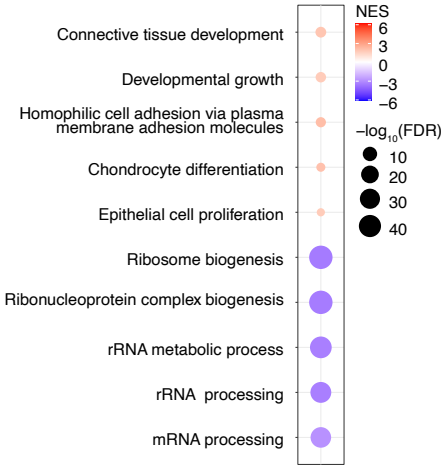

E GSEA across AluJb expression using Reactome pathway gene sets

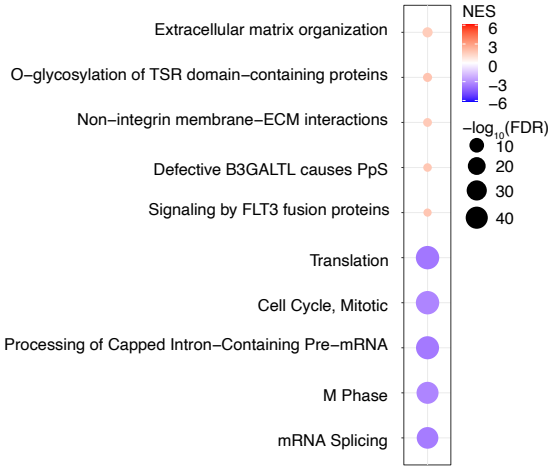

Figure 2

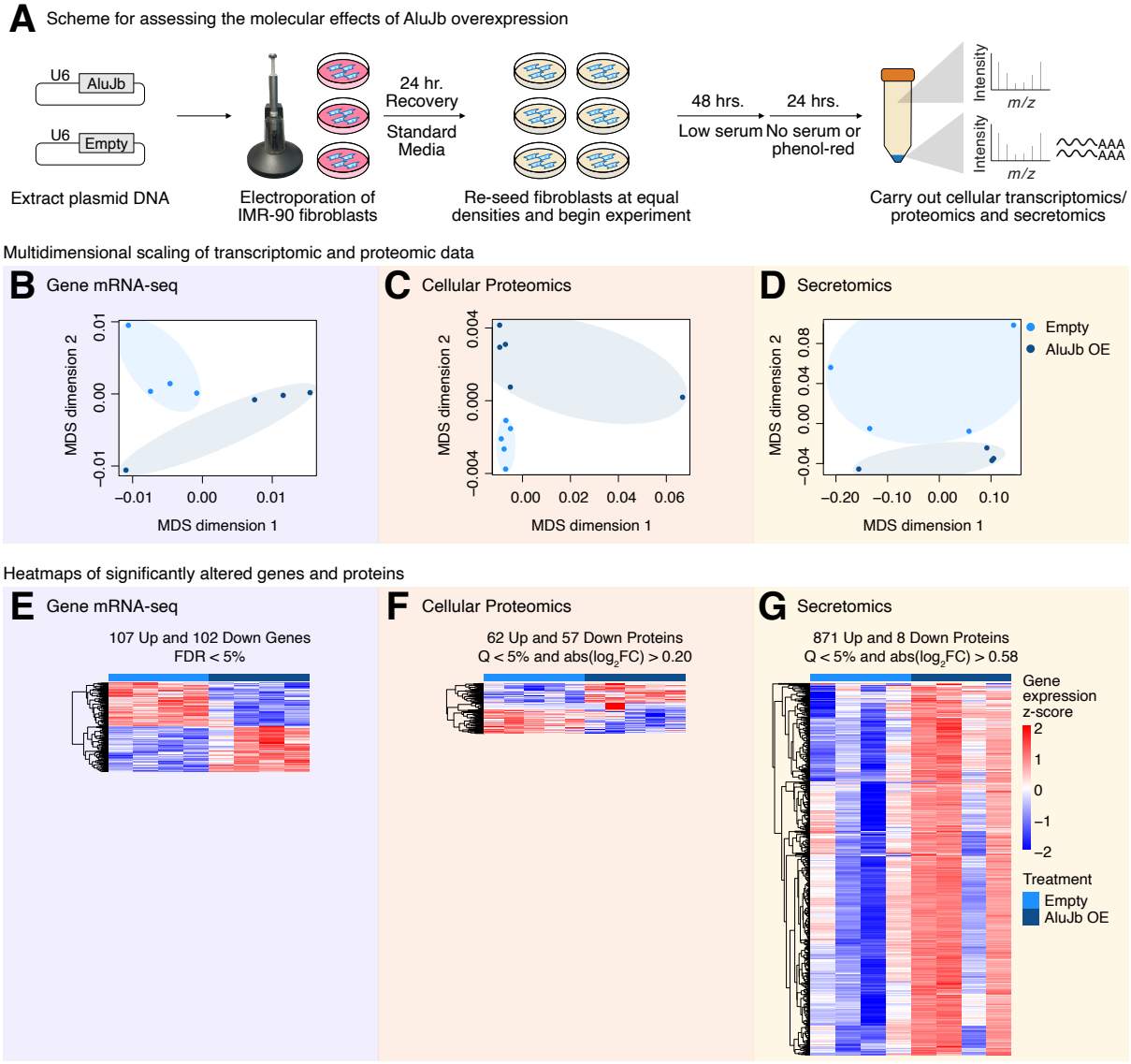
A Scheme for assessing the molecular effects of AluJb overexpression
U6
AluJb
U6
Empty
Extract plasmid DNA
Electroporation of IMR-90 fibroblasts
24 hr. Recovery
Standard Media
Re-seed fibroblasts at equal densities and begin experiment
48 hrs.
Low serum
24 hrs.
No serum or phenol-red
Intensity
m/z
Intensity
m/z
AAA
AAA
Carry out cellular transcriptomics/ proteomics and secretomics
Multidimensional scaling of transcriptomic and proteomic data
B Gene mRNA-seq
MDS dimension 2
MDS dimension 1
C Cellular Proteomics
MDS dimension 2
MDS dimension 1
D Secretomics
MDS dimension 2
MDS dimension 1
Empty
AluJb OE
Heatmaps of significantly altered genes and proteins
E Gene mRNA-seq
107 Up and 102 Down Genes
FDR < 5%
F Cellular Proteomics
62 Up and 57 Down Proteins
Q < 5% and abs(log2FC) > 0.20
G Secretomics
871 Up and 8 Down Proteins
Q < 5% and abs(log2FC) > 0.58
Gene expression z-score
Treatment
Empty
AluJb OE

Figure 3

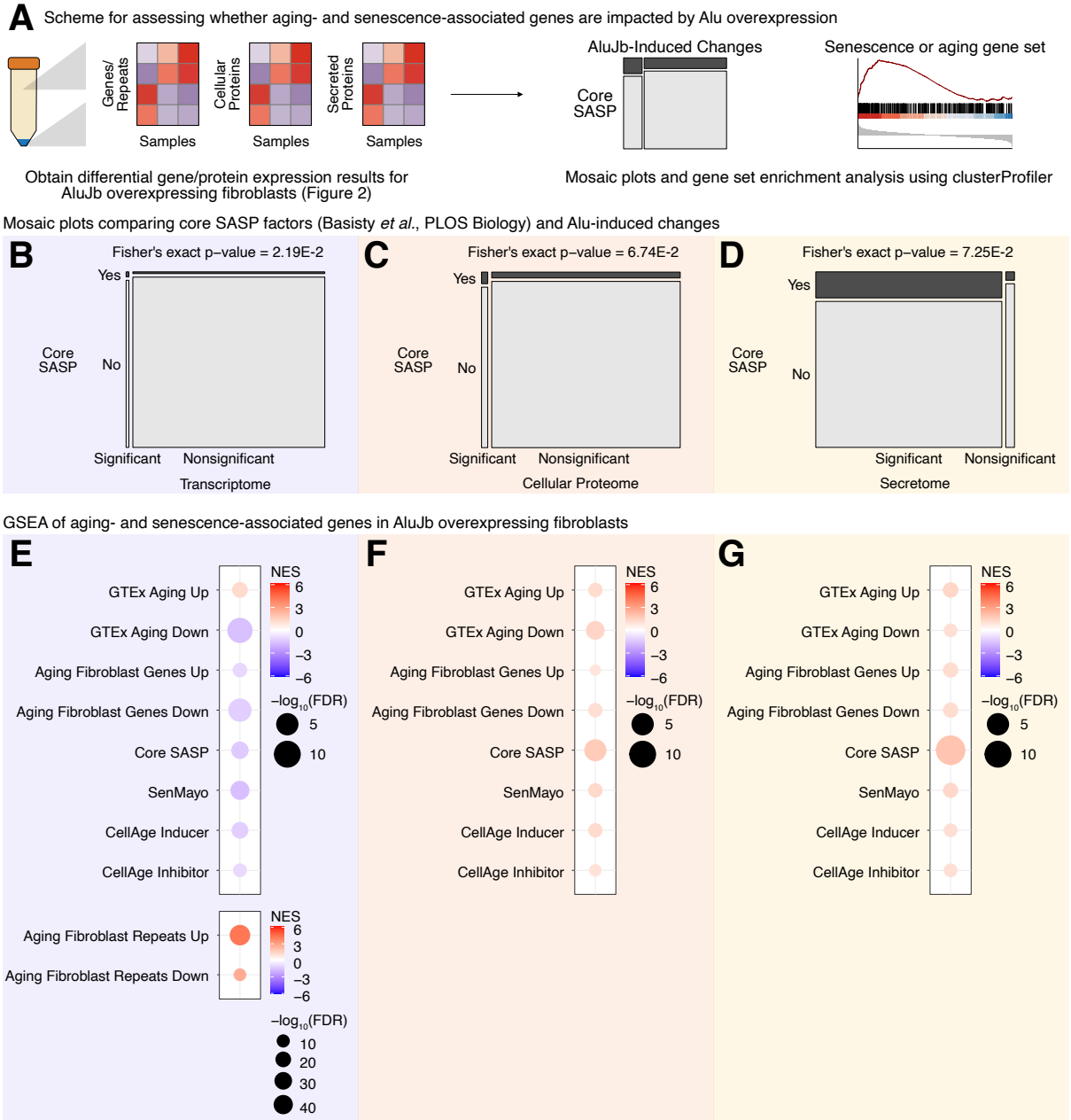
A
Scheme for assessing whether aging- and senescence-associated genes are impacted by Alu overexpression
Genes/ Repeats
Cellular Proteins
Secreted Proteins
Samples
Samples
Samples
AluJb-Induced Changes
Core SASP
Senescence or aging gene set
Obtain differential gene/protein expression results for AluJb overexpressing fibroblasts (Figure 2)
Mosaic plots and gene set enrichment analysis using clusterProfiler
Mosaic plots comparing core SASP factors (Basisty et al., PLOS Biology) and Alu-induced changes
B
Fisher's exact p–value = 2.19E-2
Yes
Core SASP
No
Significant
Nonsignificant
Transcriptome
C
Fisher's exact p–value = 6.74E-2
Yes
Core SASP
No
Significant
Nonsignificant
Cellular Proteome
D
Fisher's exact p–value = 7.25E-2
Yes
Core SASP
No
Significant
Nonsignificant
Secretome
GSEA of aging- and senescence-associated genes in AluJb overexpressing fibroblasts
E
GTEx Aging Up
GTEx Aging Down
Aging Fibroblast Genes Up
Aging Fibroblast Genes Down
Core SASP
SenMayo
CellAge Inducer
CellAge Inhibitor
NES
6
3
0
−3
−6
−log10(FDR)
5
10
Aging Fibroblast Repeats Up
Aging Fibroblast Repeats Down
NES
6
3
0
−3
−6
−log10(FDR)
10
20
30
40
F
GTEx Aging Up
GTEx Aging Down
Aging Fibroblast Genes Up
Aging Fibroblast Genes Down
Core SASP
SenMayo
CellAge Inducer
CellAge Inhibitor
NES
6
3
0
−3
−6
−log10(FDR)
5
10
G
GTEx Aging Up
GTEx Aging Down
Aging Fibroblast Genes Up
Aging Fibroblast Genes Down
Core SASP
SenMayo
CellAge Inducer
CellAge Inhibitor
NES
6
3
0
−3
−6
−log10(FDR)
5
10

Figure 4

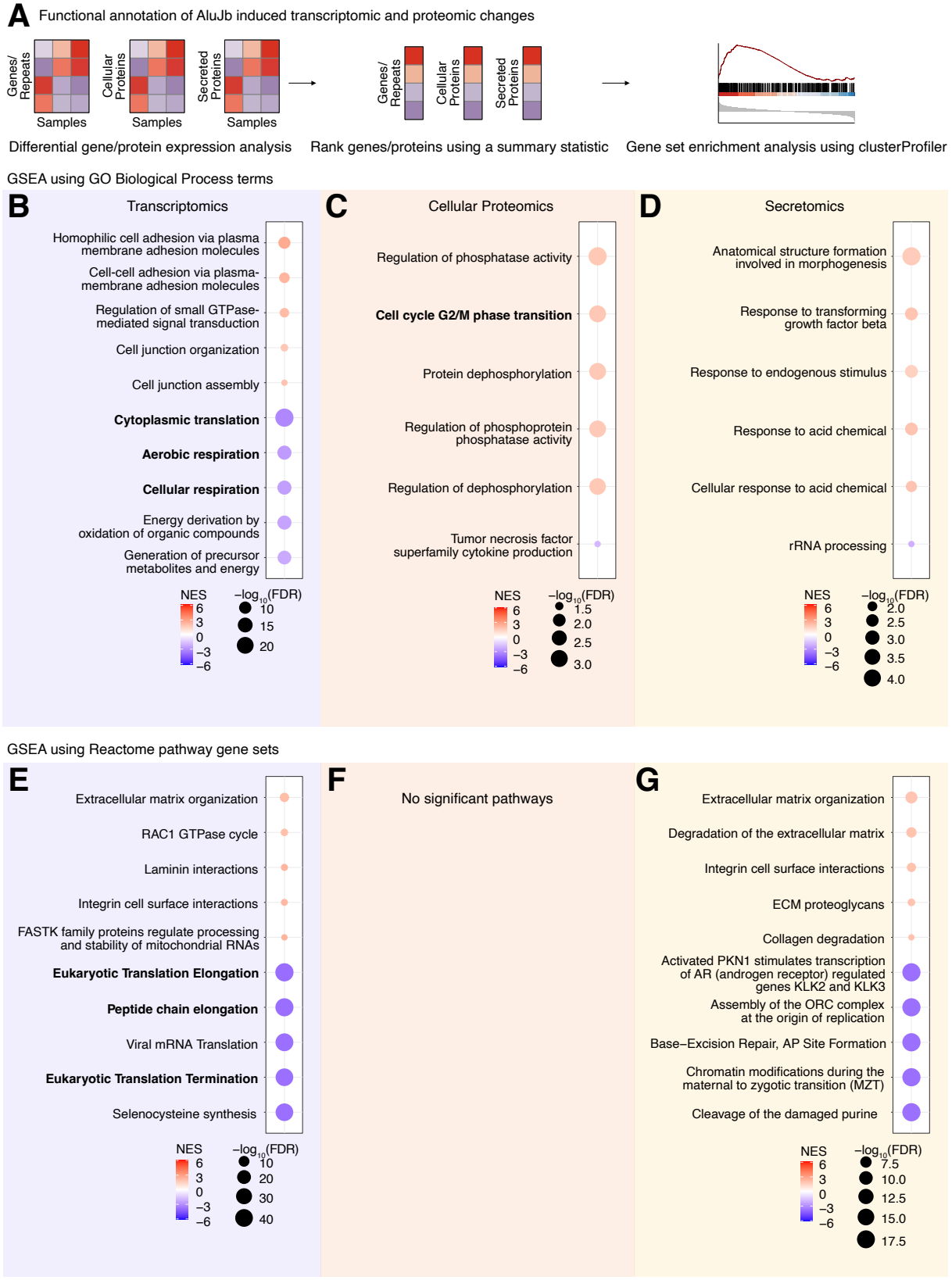
A
Functional annotation of AluJb induced transcriptomic changes
Genes/ Repeats
Cellular Proteins
Secreted Proteins
Samples
Samples
Samples
Genes/ Repeats
Cellular Proteins
Secreted Proteins
Differential gene/protein expression analysis
Rank genes/proteins using a summary statistic
Gene set enrichment analysis using clusterProfiler
GSEA using GO Biological Process terms
B
Transcriptomics
Homophilic cell adhesion via plasma membrane adhesion molecules
Cell-cell adhesion via plasma-membrane adhesion molecules
Regulation of small GTPase-mediated signal transduction
Cell junction organization
Cell junction assembly
Cytoplasmic translation
Aerobic respiration
Cellular respiration
Energy derivation by oxidation of organic compounds
Generation of precursor metabolites and energy
NES
6
3
0
−3
−6
−log10(FDR)
10
15
20
C
Cellular Proteomics
Regulation of phosphatase activity
Cell cycle G2/M phase transition
Protein dephosphorylation
Regulation of phosphoprotein phosphatase activity
Regulation of dephosphorylation
Tumor necrosis factor superfamily cytokine production
NES
6
3
0
−3
−6
−log10(FDR)
1.5
2.0
2.5
3.0
D
Secretomics
Anatomical structure formation involved in morphogenesis
Response to transforming growth factor beta
Response to endogenous stimulus
Response to acid chemical
Cellular response to acid chemical
rRNA processing
NES
6
3
0
−3
−6
−log10(FDR)
2.0
2.5
3.0
3.5
4.0
GSEA using Reactome pathway gene sets
E
Extracellular matrix organization
RAC1 GTPase cycle
Laminin interactions
Integrin cell surface interactions
FASTK family proteins regulate processing and stability of mitochondrial RNAs
Eukaryotic Translation Elongation
Peptide chain elongation
Viral mRNA Translation
Eukaryotic Translation Termination
Selenocysteine synthesis
NES
6
3
0
−3
−6
−log10(FDR)
10
20
30
40
F
No significant pathways
G
Extracellular matrix organization
Degradation of the extracellular matrix
Integrin cell surface interactions
ECM proteoglycans
Collagen degradation
Activated PKN1 stimulates transcription of AR (androgen receptor) regulated genes KLK2 and KLK3
Assembly of the ORC complex at the origin of replication
Base−Excision Repair, AP Site Formation
Chromatin modifications during the maternal to zygotic transition (MZT)
Cleavage of the damaged purine
NES
6
3
0
−3
−6
−log10(FDR)
7.5
10.0
12.5
15.0
17.5

Figure 5

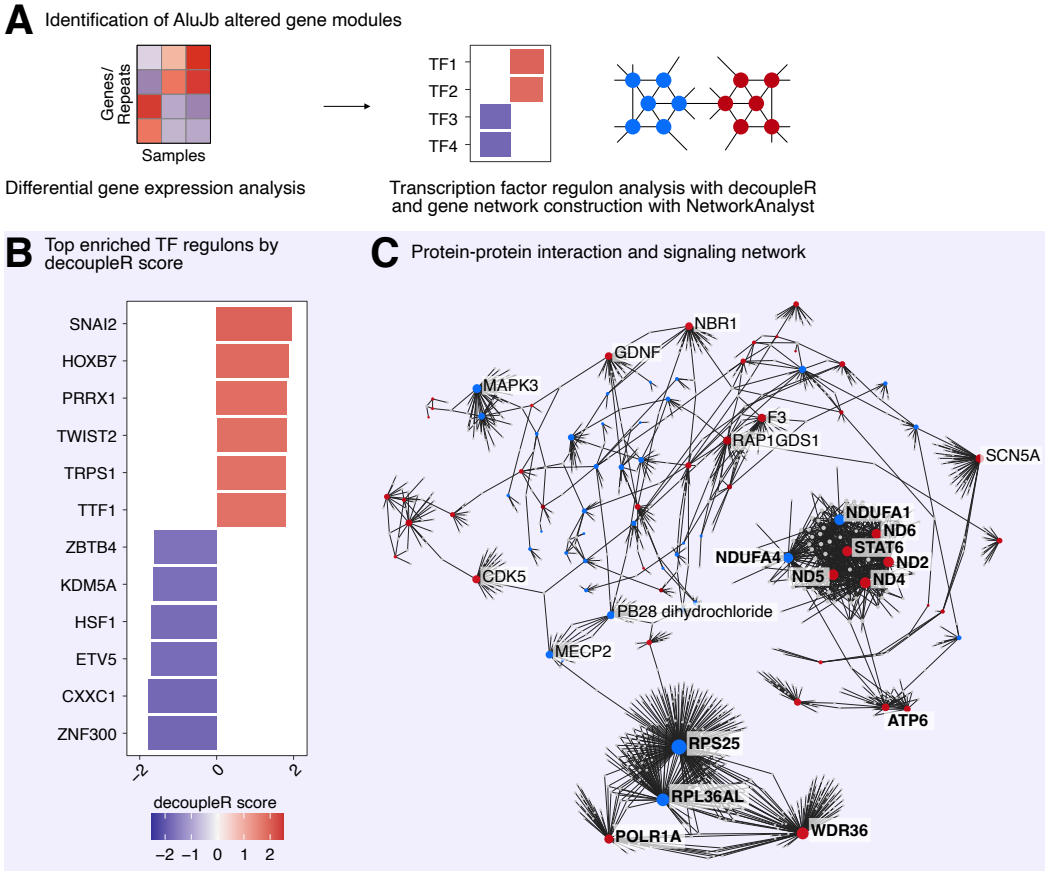
A
Identification of AluJb altered gene modules
Genes/ Repeats
Samples
Differential gene expression analysis
TF1
TF2
TF3
TF4
Transcription factor regulon analysis with decoupleR and gene network construction with NetworkAnalyst
B
Top enriched TF regulons by decoupleR score
SNAI2
HOXB7
PRRX1
TWIST2
TRPS1
TTF1
ZBTB4
KDM5A
HSF1
ETV5
CXXC1
ZNF300
-2
0
2
decoupleR score
−2 −1 0 1 2
C
Protein-protein interaction and signaling network
NBR1
GDNF
MAPK3
F3
RAP1GDS1
SCN5A
NDUFA1
ND6
STAT6
ND2
NDUFA4
ND5
ND4
CDK5
PB28 dihydrochloride
MECP2
ATP6
RPS25
RPL36AL
POLR1A
WDR36

Figure 6

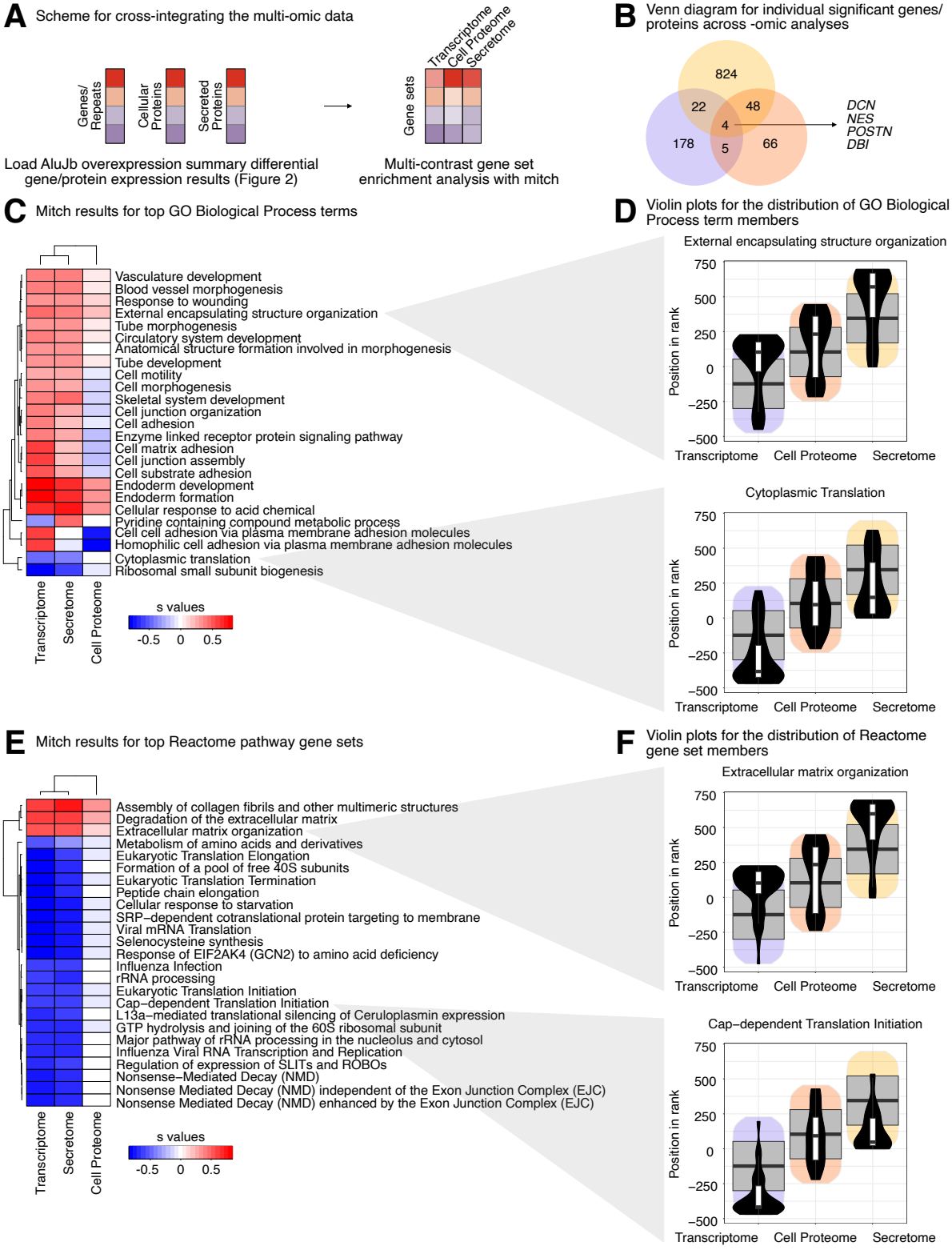
A
Scheme for cross-integrating the multi-omic data
Genes/ Repeats
Cellular Proteins
Secreted Proteins
Transcriptome
Cell Proteome
Secretome
Gene sets
Load AluJb overexpression summary differential gene/protein expression results (Figure 2)
Multi-contrast gene set enrichment analysis with mitch
B
Venn diagram for individual significant genes/ proteins across -omic analyses
824
22
48
4
178
5
66
DCN
NES
POSTN
DBI
C
Mitch results for top GO Biological Process terms
Vasculature development
Blood vessel morphogenesis
Response to wounding
External encapsulating structure organization
Tube morphogenesis
Circulatory system development
Anatomical structure formation involved in morphogenesis
Tube development
Cell motility
Cell morphogenesis
Skeletal system development
Cell junction organization
Cell adhesion
Enzyme linked receptor protein signaling pathway
Cell matrix adhesion
Cell junction assembly
Cell substrate adhesion
Endoderm development
Endoderm formation
Cellular response to acid chemical
Pyridine containing compound metabolic process
Cell cell adhesion via plasma membrane adhesion molecules
Homophilic cell adhesion via plasma membrane adhesion molecules
Cytoplasmic translation
Ribosomal small subunit biogenesis
Transcriptome
Secretome
Cell Proteome
s values
-0.5
0
0.5
D
Violin plots for the distribution of GO Biological Process term members
External encapsulating structure organization
Cytoplasmic Translation
Position in rank
750
500
250
0
−250
−500
Transcriptome
Cell Proteome
Secretome
E
Mitch results for top Reactome pathway gene sets
Assembly of collagen fibrils and other multimeric structures
Degradation of the extracellular matrix
Extracellular matrix organization
Metabolism of amino acids and derivatives
Eukaryotic Translation Elongation
Formation of a pool of free 40S subunits
Eukaryotic Translation Termination
Peptide chain elongation
Cellular response to starvation
SRP−dependent cotranslational protein targeting to membrane
Viral mRNA Translation
Selenocysteine synthesis
Response of EIF2AK4 (GCN2) to amino acid deficiency
Influenza Infection
rRNA processing
Eukaryotic Translation Initiation
Cap−dependent Translation Initiation
L13a−mediated translational silencing of Ceruloplasmin expression
GTP hydrolysis and joining of the 60S ribosomal subunit
Major pathway of rRNA processing in the nucleolus and cytosol
Influenza Viral RNA Transcription and Replication
Regulation of expression of SLITs and ROBOs
Nonsense−Mediated Decay (NMD)
Nonsense Mediated Decay (NMD) independent of the Exon Junction Complex (EJC)
Nonsense Mediated Decay (NMD) enhanced by the Exon Junction Complex (EJC)
Transcriptome
Secretome
Cell Proteome
s values
-0.5
0
0.5
F
Violin plots for the distribution of Reactome gene set members
Extracellular matrix organization
Cap−dependent Translation Initiation
Position in rank
750
500
250
0
−250
−500
Transcriptome
Cell Proteome
Secretome

Figure 7

A Scheme for assessing the effects of AluJb overexpression on cell function

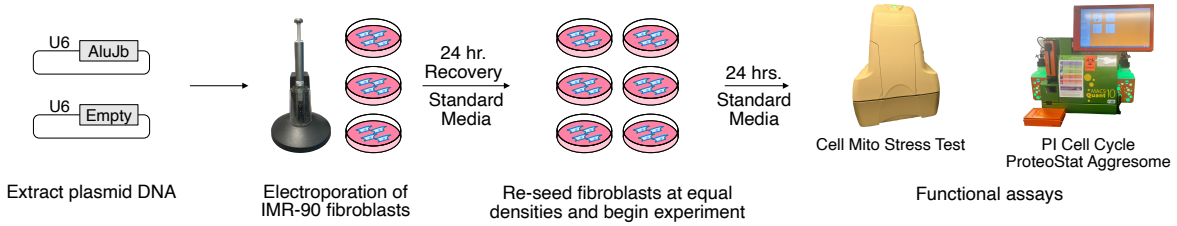

B Oxygen consumption rate (OCR) time course and sub-metrics

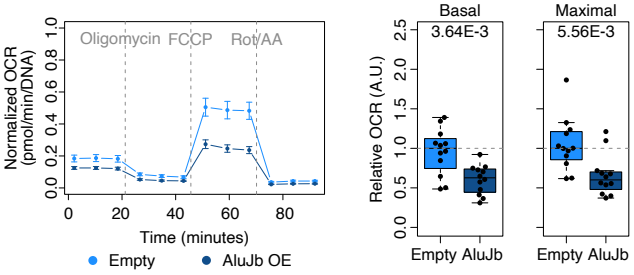

C Extracellular acidification rate (ECAR) time course

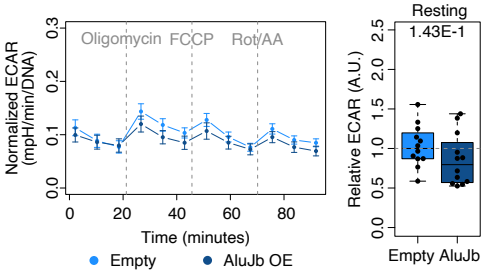

D Propidium iodide-based cell cycle phase proportions

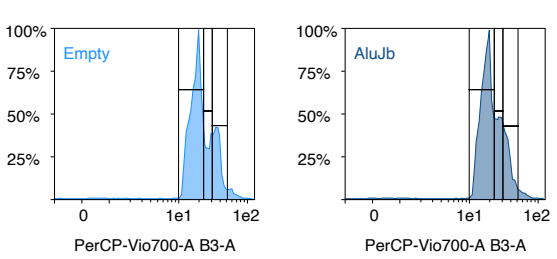

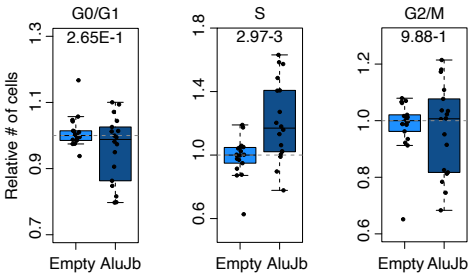

E Comparison of Proteostat aggresome MFI

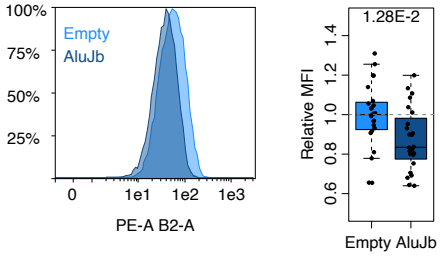

F Relationship between *AluJb* and the Hallmarks of Aging

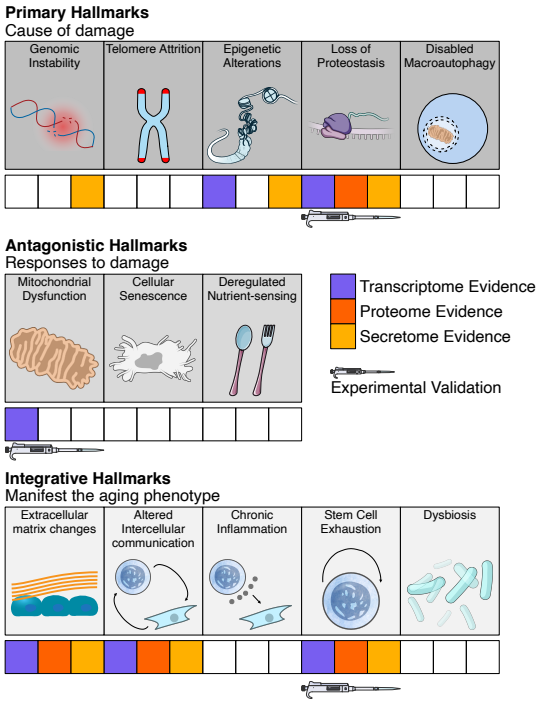

REFERENCES

Ardeljan, D., Steranka, J.P., Liu, C., Li, Z., Taylor, M.S., Taylor, M.S., Payer, L.M., Gorbounov, M., Sarnecki, J.S., Deshpande, V.*, et al.* (2020). Cell fitness screens reveal a conflict between LINE-1 retrotransposition and DNA replication. Nat Struct Mol Biol *27*, 168-178.

Avelar, R.A., Ortega, J.G., Tacutu, R., Tyler, E.J., Bennett, D., Binetti, P., Budovsky, A., Chatsirisupachai, K., Johnson, E., Murray, A.*, et al.* (2020). A multidimensional systems biology analysis of cellular senescence in aging and disease. Genome Biology *21*, 91.

Badia-i-Mompel, P., Vélez Santiago, J., Braunger, J., Geiss, C., Dimitrov, D., Müller-Dott, S., Taus, P., Dugourd, A., Holland, C.H., Ramirez Flores, R.O.*, et al.* (2022). decoupleR: ensemble of computational methods to infer biological activities from omics data. Bioinformatics Advances *2*.

Bao, W., Kojima, K.K., and Kohany, O. (2015). Repbase Update, a database of repetitive elements in eukaryotic genomes. Mobile DNA *6*, 11.

Basisty, N., Kale, A., Jeon, O.H., Kuehnemann, C., Payne, T., Rao, C., Holtz, A., Shah, S., Sharma, V., Ferrucci, L.*, et al.* (2020). A proteomic atlas of senescence-associated secretomes for aging biomarker development. PLOS Biology *18*, e3000599.

Benayoun, B.A., Pollina, E., Singh, P.P., Mahmoudi, S., Harel, I., Casey, K., Dulken, B., Kundaje, A., and Brunet, A. (2018). Remodeling of epigenome and transcriptome landscapes with aging in mice reveals widespread induction of inflammatory responses. bioRxiv, 336172.

Bennett, E.A., Keller, H., Mills, R.E., Schmidt, S., Moran, J.V., Weichenrieder, O., and Devine, S.E. (2008). Active Alu retrotransposons in the human genome. Genome research *18*, 1875-1883.

Blair, L.P., Cao, J., Zou, M.R., Sayegh, J., and Yan, Q. (2011). Epigenetic Regulation by Lysine Demethylase 5 (KDM5) Enzymes in Cancer. Cancers (Basel) *3*, 1383-1404.

Bravo, J.I., Mizrahi, C.R., Kim, S., Zhang, L., Suh, Y., and Benayoun, B.A. (2024). An eQTL-based approach reveals candidate regulators of LINE-1 RNA levels in lymphoblastoid cells. PLOS Genetics *20*, e1011311.

Bravo, J.I., Nozownik, S., Danthi, P.S., and Benayoun, B.A. (2020). Transposable elements, circular RNAs and mitochondrial transcription in age-related genomic regulation. Development *147*.

Bruderer, R., Bernhardt, O.M., Gandhi, T., Xuan, Y., Sondermann, J., Schmidt, M., Gomez-Varela, D., and Reiter, L. (2017). Optimization of Experimental Parameters in Data-Independent Mass Spectrometry Significantly Increases Depth and Reproducibility of Results. Molecular & cellular proteomics : MCP *16*, 2296-2309.

698 Bujisic, B., Lee, H.-G., Xu, L., Weissbein, U., Rivera, C., Topisirovic, I., and Lee, J.T. (2025). 7SL
699 RNA and signal recognition particle orchestrate a global cellular response to acute thermal stress.
700 Nature Communications *16*, 1630.
701 Burger, T. (2018). Gentle Introduction to the Statistical Foundations of False Discovery Rate in
702 Quantitative Proteomics. Journal of Proteome Research *17*, 12-22.
703 Cantarella, S., Carnevali, D., Morselli, M., Conti, A., Pellegrini, M., Montanini, B., and Dieci, G.
704 (2019). Alu RNA Modulates the Expression of Cell Cycle Genes in Human Fibroblasts. Int J Mol
705 Sci *20*.
706 Chen, H., Zheng, X., Xiao, D., and Zheng, Y. (2016). Age-associated de-repression of
707 retrotransposons in the Drosophila fat body, its potential cause and consequence. Aging Cell *15*,
708 542-552.
709 Chen, S., Zhou, Y., Chen, Y., and Gu, J. (2018). fastp: an ultra-fast all-in-one FASTQ
710 preprocessor. Bioinformatics *34*, i884-i890.
711 Collins, B.C., Hunter, C.L., Liu, Y., Schilling, B., Rosenberger, G., Bader, S.L., Chan, D.W.,
712 Gibson, B.W., Gingras, A.-C., Held, J.M.*, et al.* (2017). Multi-laboratory assessment of
713 reproducibility, qualitative and quantitative performance of SWATH-mass spectrometry. Nature
714 communications *8*, 291-291.
715 De Cecco, M., Criscione, S.W., Peckham, E.J., Hillenmeyer, S., Hamm, E.A., Manivannan, J.,
716 Peterson, A.L., Kreiling, J.A., Neretti, N., and Sedivy, J.M. (2013a). Genomes of replicatively
717 senescent cells undergo global epigenetic changes leading to gene silencing and activation of
718 transposable elements. Aging Cell *12*, 247-256.
719 De Cecco, M., Criscione, S.W., Peterson, A.L., Neretti, N., Sedivy, J.M., and Kreiling, J.A.
720 (2013b). Transposable elements become active and mobile in the genomes of aging mammalian
721 somatic tissues. Aging (Albany NY) *5*, 867-883.
722 De Cecco, M., Ito, T., Petrashen, A.P., Elias, A.E., Skvir, N.J., Criscione, S.W., Caligiana, A.,
723 Brocculi, G., Adney, E.M., Boeke, J.D.*, et al.* (2019). L1 drives IFN in senescent cells and
724 promotes age-associated inflammation. Nature *566*, 73-78.
725 Dennis, S., Sheth, U., Feldman, J.L., English, K.A., and Priess, J.R. (2012). C. elegans Germ
726 Cells Show Temperature and Age-Dependent Expression of Cer1, a Gypsy/Ty3-Related
727 Retrotransposon. PLOS Pathogens *8*, e1002591.
728 Dewannieux, M., Esnault, C., and Heidmann, T. (2003). LINE-mediated retrotransposition of
729 marked Alu sequences. Nature Genetics *35*, 41-48.

730 Di Ruocco, F., Basso, V., Rivoire, M., Mehlen, P., Ambati, J., De Falco, S., and Tarallo, V. (2018).
731 Alu RNA accumulation induces epithelial-to-mesenchymal transition by modulating miR-566 and
732 is associated with cancer progression. Oncogene *37*, 627-637.
733 Dobin, A., Davis, C.A., Schlesinger, F., Drenkow, J., Zaleski, C., Jha, S., Batut, P., Chaisson, M.,
734 and Gingeras, T.R. (2012). STAR: ultrafast universal RNA-seq aligner. Bioinformatics *29*, 15-21.
735 Escher, C., Reiter, L., MacLean, B., Ossola, R., Herzog, F., Chilton, J., MacCoss, M.J., and
736 Rinner, O. (2012). Using iRT, a normalized retention time for more targeted measurement of
737 peptides. Proteomics *12*, 1111-1121.
738 Fleischer, J.G., Schulte, R., Tsai, H.H., Tyagi, S., Ibarra, A., Shokhirev, M.N., Huang, L., Hetzer,
739 M.W., and Navlakha, S. (2018). Predicting age from the transcriptome of human dermal
740 fibroblasts. Genome Biology *19*, 221.
741 Frankish, A., Diekhans, M., Ferreira, A.-M., Johnson, R., Jungreis, I., Loveland, J., Mudge, J.M.,
742 Sisu, C., Wright, J., Armstrong, J.*, et al.* (2018). GENCODE reference annotation for the human
743 and mouse genomes. Nucleic Acids Research *47*, D766-D773.
744 Gao, Z., Herrera-Carrillo, E., and Berkhout, B. (2018). Delineation of the Exact Transcription
745 Termination Signal for Type 3 Polymerase III. Molecular Therapy - Nucleic Acids *10*, 36-44.
746 Gillet, L.C., Navarro, P., Tate, S., Röst, H., Selevsek, N., Reiter, L., Bonner, R., and Aebersold,
747 R. (2012). Targeted data extraction of the MS/MS spectra generated by data-independent
748 acquisition: a new concept for consistent and accurate proteome analysis. Molecular & cellular
749 proteomics : MCP *11*, O111.016717-O016111.016717.
750 Guo, C., Jeong, H.-H., Hsieh, Y.-C., Klein, H.-U., Bennett, D.A., De Jager, P.L., Liu, Z., and
751 Shulman, J.M. (2018). Tau Activates Transposable Elements in Alzheimer’s Disease.
752 Cell Reports *23*, 2874-2880.
753 Iskow, R.C., McCabe, M.T., Mills, R.E., Torene, S., Pittard, W.S., Neuwald, A.F., Van Meir, E.G.,
754 Vertino, P.M., and Devine, S.E. (2010). Natural Mutagenesis of Human Genomes by Endogenous
755 Retrotransposons. Cell *141*, 1253-1261.
756 Jia, K., Cui, C., Gao, Y., Zhou, Y., and Cui, Q. (2018). An analysis of aging-related genes derived
757 from the Genotype-Tissue Expression project (GTEx). Cell Death Discovery *4*, 91.
758 Jin, Y., Tam, O.H., Paniagua, E., and Hammell, M. (2015). TEtranscripts: a package for including
759 transposable elements in differential expression analysis of RNA-seq datasets. Bioinformatics *31*,
760 3593-3599.
761 Kaspi, A., and Ziemann, M. (2020). mitch: multi-contrast pathway enrichment for multi-omics and
762 single-cell profiling data. BMC Genomics *21*, 447.

763 Kerur, N., Fukuda, S., Banerjee, D., Kim, Y., Fu, D., Apicella, I., Varshney, A., Yasuma, R., Fowler,
764 B.J., Baghdasaryan, E.*, et al.* (2017). cGAS drives noncanonical-inflammasome activation in age-
765 related macular degeneration. Nature Medicine *24*, 50.
766 Kidwell, M.G. (2002). Transposable elements and the evolution of genome size in eukaryotes.
767 Genetica *115*, 49-63.
768 Kiuchi, M., Onodera, A., Kokubo, K., Ichikawa, T., Morimoto, Y., Kawakami, E., Takayama, N.,
769 Eto, K., Koseki, H., Hirahara, K.*, et al.* (2021). The Cxxc1 subunit of the Trithorax complex directs
770 epigenetic licensing of CD4+ T cell differentiation. J Exp Med *218*.
771 Kroemer, G., Maier, A.B., Cuervo, A.M., Gladyshev, V.N., Ferrucci, L., Gorbunova, V., Kennedy,
772 B.K., Rando, T.A., Seluanov, A., Sierra, F.*, et al.* (2025). From geroscience to precision
773 geromedicine: Understanding and managing aging. Cell *188*, 2043-2062.
774 Lander, E.S., Linton, L.M., Birren, B., Nusbaum, C., Zody, M.C., Baldwin, J., Devon, K., Dewar,
775 K., Doyle, M., FitzHugh, W.*, et al.* (2001). Initial sequencing and analysis of the human genome.
776 Nature *409*, 860-921.
777 LaRocca, T.J., Cavalier, A.N., and Wahl, D. (2020). Repetitive elements as a transcriptomic
778 marker of aging: Evidence in multiple datasets and models. Aging Cell *19*, e13167.
779 Lee, K.-W., Yeo, S.-Y., Gong, J.-R., Koo, O.-J., Sohn, I., Lee, W.Y., Kim, H.C., Yun, S.H., Cho,
780 Y.B., Choi, M.-A.*, et al.* (2022). PRRX1 is a master transcription factor of stromal fibroblasts for
781 myofibroblastic lineage progression. Nature Communications *13*, 2793.
782 Li, W., Prazak, L., Chatterjee, N., Grüninger, S., Krug, L., Theodorou, D., and Dubnau, J. (2013).
783 Activation of transposable elements during aging and neuronal decline in Drosophila. Nature
784 neuroscience *16*, 529.
785 Liberzon, A., Birger, C., Thorvaldsdóttir, H., Ghandi, M., Mesirov, J.P., and Tamayo, P. (2015).
786 The Molecular Signatures Database (MSigDB) hallmark gene set collection. Cell Syst *1*, 417-425.
787 Love, M.I., Huber, W., and Anders, S. (2014). Moderated estimation of fold change and dispersion
788 for RNA-seq data with DESeq2. Genome Biology *15*, 550.
789 Luca, C.D., Guadagni, F., Sinibaldi-Vallebona, P., Sentinelli, S., Gallucci, M., Hoffmann, A.,
790 Schumann, G.G., Spadafora, C., and Sciamanna, I. (2015). Enhanced expression of LINE-1-
791 encoded ORF2 protein in early stages of colon and prostate transformation. Oncotarget *7*.
792 Mao, Z., Feng, M., Li, Z., Zhou, M., Xu, L., Pan, K., Wang, S., Su, W., and Zhang, W. (2021).
793 ETV5 Regulates Hepatic Fatty Acid Metabolism Through PPAR Signaling Pathway. Diabetes *70*,
794 214-226.

795 Milacic, M., Beavers, D., Conley, P., Gong, C., Gillespie, M., Griss, J., Haw, R., Jassal, B.,
796 Matthews, L., May, B.*, et al.* (2023). The Reactome Pathway Knowledgebase 2024. Nucleic Acids
797 Research *52*, D672-D678.
798 Müller-Dott, S., Tsirvouli, E., Vazquez, M., Ramirez Flores, Ricardo O., Badia-i-Mompel, P.,
799 Fallegger, R., Türei, D., Lægreid, A., and Saez-Rodriguez, J. (2023). Expanding the coverage of
800 regulons from high-confidence prior knowledge for accurate estimation of transcription factor
801 activities. Nucleic Acids Research *51*, 10934-10949.
802 Neri, F., Basisty, N., Desprez, P.-Y., Campisi, J., and Schilling, B. (2021). Quantitative Proteomic
803 Analysis of the Senescence-Associated Secretory Phenotype by Data-Independent Acquisition.
804 Current Protocols *1*, e32.
805 Nyathi, Y., Wilkinson, B.M., and Pool, M.R. (2013). Co-translational targeting and translocation of
806 proteins to the endoplasmic reticulum. Biochimica et Biophysica Acta (BBA) - Molecular Cell
807 Research *1833*, 2392-2402.
808 Pabis, K., Barardo, D., Sirbu, O., Selvarajoo, K., Gruber, J., and Kennedy, B.K. (2024). A
809 concerted increase in readthrough and intron retention drives transposon expression during aging
810 and senescence. eLife *12*, RP87811.
811 Pincus, D. (2020). Regulation of Hsf1 and the Heat Shock Response. Adv Exp Med Biol *1243*,
812 41-50.
813 Ritchie, M.E., Phipson, B., Wu, D., Hu, Y., Law, C.W., Shi, W., and Smyth, G.K. (2015). limma
814 powers differential expression analyses for RNA-sequencing and microarray studies. Nucleic
815 Acids Research *43*, e47-e47.
816 Rodić, N., Sharma, R., Sharma, R., Zampella, J., Dai, L., Taylor, M.S., Hruban, R.H., Iacobuzio-
817 Donahue, C.A., Maitra, A., Torbenson, M.S.*, et al.* (2014). Long Interspersed Element-1 Protein
818 Expression Is a Hallmark of Many Human Cancers. The American Journal of Pathology *184*,
819 1280-1286.
820 Rubin, C.M., Houck, C.M., Deininger, P.L., Friedmann, T., and Schmid, C.W. (1980). Partial
821 nucleotide sequence of the 300-nucleotide interspersed repeated human DNA sequences. Nature
822 *284*, 372-374.
823 Sampathkumar, N.K., Bravo, J.I., Chen, Y., Danthi, P.S., Donahue, E.K., Lai, R.W., Lu, R.,
824 Randall, L.T., Vinson, N., and Benayoun, B.A. (2020). Widespread sex dimorphism in aging and
825 age-related diseases. Hum Genet *139*, 333-356.
826 Saul, D., Kosinsky, R.L., Atkinson, E.J., Doolittle, M.L., Zhang, X., LeBrasseur, N.K., Pignolo,
827 R.J., Robbins, P.D., Niedernhofer, L.J., Ikeno, Y.*, et al.* (2022). A new gene set identifies

828 senescent cells and predicts senescence-associated pathways across tissues. Nature
829 Communications *13*, 4827.
830 Subramanian, A., Tamayo, P., Mootha, V.K., Mukherjee, S., Ebert, B.L., Gillette, M.A., Paulovich,
831 A., Pomeroy, S.L., Golub, T.R., Lander, E.S.*, et al.* (2005). Gene set enrichment analysis: A
832 knowledge-based approach for interpreting genome-wide expression profiles. Proceedings of the
833 National Academy of Sciences *102*, 15545-15550.
834 Sun, W., Samimi, H., Gamez, M., Zare, H., and Frost, B. (2018). Pathogenic tau-induced piRNA
835 depletion promotes neuronal death through transposable element dysregulation in
836 neurodegenerative tauopathies. Nature neuroscience *21*, 1038-1048.
837 Ullu, E., and Tschudi, C. (1984). Alu sequences are processed 7SL RNA genes. Nature *312*, 171-
838 172.
839 Venter, J.C., Adams, M.D., Myers, E.W., Li, P.W., Mural, R.J., Sutton, G.G., Smith, H.O., Yandell,
840 M., Evans, C.A., Holt, R.A.*, et al.* (2001). The Sequence of the Human Genome. Science *291*,
841 1304-1351.
842 Vogel, C., and Marcotte, E.M. (2012). Insights into the regulation of protein abundance from
843 proteomic and transcriptomic analyses. Nature Reviews Genetics *13*, 227-232.
844 Wallace, N., Wagstaff, B.J., Deininger, P.L., and Roy-Engel, A.M. (2008). LINE-1 ORF1 protein
845 enhances Alu SINE retrotransposition. Gene *419*, 1-6.
846 Walter, P., and Blobel, G. (1982). Signal recognition particle contains a 7S RNA essential for
847 protein translocation across the endoplasmic reticulum. Nature *299*, 691-698.
848 Wang, J., Geesman, G.J., Hostikka, S.L., Atallah, M., Blackwell, B., Lee, E., Cook, P.J., Pasaniuc,
849 B., Shariat, G., Halperin, E.*, et al.* (2011). Inhibition of activated pericentromeric SINE/Alu repeat
850 transcription in senescent human adult stem cells reinstates self-renewal. Cell Cycle *10*, 3016-
851 3030.
852 Wild, K., Weichenrieder, O., Strub, K., Sinning, I., and Cusack, S. (2002). Towards the structure
853 of the mammalian signal recognition particle. Current Opinion in Structural Biology *12*, 72-81.
854 Wood, J.G., Jones, B.C., Jiang, N., Chang, C., Hosier, S., Wickremesinghe, P., Garcia, M.,
855 Hartnett, D.A., Burhenn, L., Neretti, N.*, et al.* (2016). Chromatin-modifying genetic interventions
856 suppress age-associated transposable element activation and extend life span in
857 Drosophila. Proceedings of the National Academy of Sciences *113*, 11277-11282.
858 Wu, T., Hu, E., Xu, S., Chen, M., Guo, P., Dai, Z., Feng, T., Zhou, L., Tang, W., Zhan, L.*, et al.*
859 (2021). clusterProfiler 4.0: A universal enrichment tool for interpreting omics data. The Innovation
860 *2*, 100141.

861 Xia, J., Benner, M.J., and Hancock, R.E.W. (2014). NetworkAnalyst - integrative approaches for
862 protein–protein interaction network analysis and visual exploration. Nucleic Acids Research *42*,
863 W167-W174.
864 Xia, J., Gill, E.E., and Hancock, R.E.W. (2015). NetworkAnalyst for statistical, visual and network-
865 based meta-analysis of gene expression data. Nature Protocols *10*, 823-844.
866 Yamada, K., Kaneko, H., Shimizu, H., Suzumura, A., Namba, R., Takayama, K., Ito, S., Sugimoto,
867 M., and Terasaki, H. (2020). Lamivudine Inhibits Alu RNA-induced Retinal Pigment Epithelium
868 Degeneration via Anti-inflammatory and Anti-senescence Activities. Translational Vision Science
869 & Technology *9*, 1-1.
870 Zhou, G., Soufan, O., Ewald, J., Hancock, R.E.W., Basu, N., and Xia, J. (2019). NetworkAnalyst
871 3.0: a visual analytics platform for comprehensive gene expression profiling and meta-analysis.
872 Nucleic Acids Research *47*, W234-W241.

873

874 **STAR★METHODS**

875 KEY RESOURCES TABLE

REAGENT OR RESOURCE	SOURCE	IDENTIFIER
Bacterial and virus strains		
NEB Turbo Competent *E. coli*	New England Biolabs	C2984H
Chemicals, peptides, and recombinant proteins		
Propidium Iodide	Alfa Aesar	J66584
PureLink RNase A	Invitrogen	12091021
Triton X-100	MP	194854
Critical commercial assays		
Seahorse XF Cell Mito Stress Test Kit	Agilent	103015-100
Seahorse XF Pro M Cell Culture Microplate	Agilent	103774-100
Seahorse XF Base Medium	Agilent	102353-100
PROTEOSTAT Aggresome Detection Kit	Enzo	ENZ-51035-K100
Deposited data		
GRCh38 GENCODE release 44 annotations	(Frankish et al., 2018)	
Aging human primary fibroblast mRNA-seq	(Fleischer et al., 2018)	GSE113957
IMR-90 *AluJb* overexpression mRNA-seq	This study	PRJNA1008694

IMR-90 *AluJb* overexpression MS data	This study	MassIVE ID: MSV000097822; ProteomeXchange ID: PXD063739
IMR-90 *AluJb* overexpression functional data	This study	Figshare DOI: 10.6084/m9.figshare.28928147
IMR-90 *AluS* stable overexpression gene set	(Cantarella et al., 2019)	
Gene Ontology (GO) Biological Process gene sets v2024.1.Hs	Molecular Signature Database	
Reactome v92 pathway gene sets	Reactome	
Core SASP factors gene set	(Basisty et al., 2020)	
SenMayo gene set	(Saul et al., 2022)	
CellAge build 3 gene sets	(Avelar et al., 2020)	
GTEx aging-associated genes	(Jia et al., 2018)	
Experimental models: Cell lines		
IMR-90 (received at Passage 4 with PDL 9.74)	Coriell Institute	I90-83; RRID: CVCL_0347
Oligonucleotides		
TAAGCA_HindIII_U6_For 5'-TAAGCAAAGCTTgagggcctatttcccatgattcct-3'	This study	

TAAGCA_EcoRI_U6_R 5’-TAAGCAGAATTCgtcctttccacaagatatataaag-3’	This study	
AluJB_exten_U6_R 5’-ccgcgcccggcCgtcctttccacaagatatataaag-3’	This study	
U6_exten_AluJB_F 5’-ctttatatatcttgtggaaaggacGgccgggcgcgg-3’	This study	
TAAGCA_EcoRI_5T_AluJB_R 5’-TAAGCAGAATTCaaaaatgagacagggtctcgctctgt-3’	This study	
AluJb_qPCR4 F 5’-ACAAAAATTAGCCGGGCGTG-3’ AluJb_qPCR4 R 5’-CAGGGTTTTCCCAGTCACGA-3’	This study	
Recombinant DNA		
pLKO.1 cloning vector	Addgene	RRID: Addgene_10878
pUC19 cloning vector	New England Biolabs	N3041S
pUC57_AluJb	This study	
pUC19-U6	This study	RRID: Addgene_240313

pUC19-U6_AluJb	This study	RRID: Addgene_240314
Software and algorithms		
R v4.3.3	R Foundation	
fastp v0.20.1	(Chen et al., 2018)	https://github.com/OpenGene/fastp
fastqc v0.11.9	Simon Andrews	https://github.com/s-andrews/FastQC
STAR v2.7.3a	(Dobin et al., 2012)	https://github.com/alexdobin/STAR
TEtranscripts v2.1.4	(Jin et al., 2015)	https://github.com/mhammell-laboratory/TEtranscripts
TElocal v1.1.1	(Jin et al., 2015)	https://github.com/mhammell-laboratory/TElocal
DESeq2 v1.42.1	(Love et al., 2014)	
Limma v3.58.1	(Ritchie et al., 2015).	
clusterProfiler v4.10.1	(Wu et al., 2021)	
mitch v1.14.0	(Kaspi and Ziemann, 2020)	https://github.com/markziemann/mitch
decoupleR v2.8.0	(Badia-i-Mompel et al., 2022)	

Other		
AccuPrime *Pfx* DNA polymerase	Invitrogen	12344024
Nucleospin Gel and PCR Cleanup Kit	Macherey-Nagel	740609.50
Quick Ligation Kit	NEB	M2200S
Minimum essential medium with Earle's salts without L-glutamine	Corning	15-010-CV
Fetal bovine serum	Sigma-Aldrich	F0926-500ML
Non-essential amino acids	Quality Biological	116-078-721
Penicillin-Streptomycin-Glutamine	Corning	30-009-CI
Dulbecco's phosphate-buffered saline	Corning	21-031-CV
0.25% trypsin	HyClone	95053-258
Minimum essential medium with Earle's salts without L-glutamine or phenol red	Corning	17-305-CV
Target2 0.45 μm polyvinylidene fluoride syringe filters	Thermo Scientific	F2500-5
0.05% trypsin	Corning	25-052-CI
Nucleobond Xtra Midi Plus EF kit	Macherey-Nagel	740422.50
Neon Transfection System 100 μL Kit	Invitrogen	MPK10096
Direct-zol RNA Miniprep kit	Zymo Research	R2052
Maxima H Minus cDNA Synthesis Master Mix with dsDNase	Thermo Scientific	M1682
MyTaq HS Red Mix	Meridian Bioscience	BIO-25048

876

877

878

879

880 EXPERIMENTAL MODEL AND STUDY PARTICIPANT DETAILS

881 **Cell lines and cell culture conditions**

882 IMR-90 (Coriell cat. I90-83, RRID: CVCL_0347) human female embryonic fibroblast cells
883 were purchased from the Coriell Institute. Cells were maintained in Minimum Essential Medium
884 (MEM) containing Earle's salts (Corning cat. 15-010-CV), 15% fetal bovine serum (FBS, Sigma-
885 Aldrich cat. F0926-500ML), 1X non-essential amino acids (NEAA, Quality Biological cat. 116-078-
886 721), and 1X Penicillin-Streptomycin-Glutamine (Corning cat. 30-009-CI). Cells were cultured in
887 a humidified incubator at 37°C and 5% CO_2, subculturing cells 1:6 once they reached ~90%
888 confluency. All cells used were maintained below passage 30 and routinely tested for
889 mycoplasma contamination using the PlasmoTest Mycoplasma Detection Kit (InvivoGen). The
890 identity and purity of cells used in this study were verified using ATCC's Human Cell STR Profiling
891 Service (ATCC 135-XV).

892

893 METHOD DETAILS

894 **Plasmid Construction**

895 The empty pLKO.1 cloning vector, which contains the U6 promoter, was a gift from David
896 Root (Addgene plasmid #10878; http://n2t.net/addgene:10878; RRID: Addgene_10878). The
897 empty pUC19 cloning vector was purchased from New England Biolabs (NEB; cat. N3041S).

898 The *AluJb* overexpression construct was generated by overlap extension polymerase
899 chain reaction (PCR). To begin, the *AluJb* consensus sequence was obtained from Repbase (Bao
900 et al., 2015) and submitted to Genewiz for gene synthesis, yielding pUC57_AluJb. Next, the U6
901 promoter was amplified from pLKO.1 using primers TAAGCA_HindIII_U6_For and
902 AluJB_exten_U6_R, and *AluJb* was amplified from pUC57_AluJb using primers
903 U6_exten_AluJB_F and TAAGCA_EcoRI_5T_AluJB_R. Importantly, the *AluJb* amplification
904 primers introduced a stretch of 5 thymidine residues in the *AluJb* 3' terminal region to act as a
905 minimal RNA polymerase III termination signal (Gao et al., 2018). A first round of PCRs was
906 carried out using AccuPrime *Pfx* DNA polymerase (Invitrogen cat. 12344024) in a Biorad C1000
907 Touch Thermal Cycler with these steps: initial denaturation (95°C, 2 minutes) and 35 cycles of
908 denaturation (95°C, 15 seconds), annealing (55°C, 30 seconds), and extension (68°C, 60
909 seconds). The PCR products were run on an agarose gel, the amplicons of the expected size
910 were excised, and the DNA was purified using the Nucleospin Gel and PCR Cleanup Kit
911 (Macherey-Nagel item 740609.50). After, equimolar amounts of the U6 amplicon and the *AluJb*

912 amplicon were mixed together with *Pfx* DNA polymerase, in order to fuse the U6 promoter with
913 *AluJb* through a second round of PCRs (initial denaturation at 98°C for 30 seconds and 7 cycles
914 of denaturation at 98°C for 10 second, annealing at 72°C for 30 second, and extension at 72°C
915 for 15 seconds). An aliquot of the resulting PCR products was used as a template for a third round
916 of PCRs to amplify the final 541 base pair U6_AluJb fusion product using primers
917 TAAGCA_HindIII_U6_For and TAAGCA_EcoRI_5T_AluJB_R. This third set of PCRs was run
918 under the same conditions as the first round but only for 25 cycles and using an annealing
919 temperature of 60°C. Again, PCR products were run on an agarose gel and purified as before.
920 Then, the pUC19 backbone and purified U6_AluJb amplicon were both digested with HindIII-HF
921 and EcoRI-HF, the desired digestion products were purified from an agarose gel, and the
922 backbone and insert were ligated together using the Quick Ligation Kit (NEB cat. M2200S),
923 generating pUC19-U6_AluJb. NEB Turbo competent *Escherichia coli* (*E. coli*) (cat. C2984H) were
924 transformed with the ligation product using the manufacturer recommended high efficiency
925 transformation protocol. The final U6_AluJb fusion on the pUC19 backbone was sequence
926 verified using Sanger sequencing. For a control plasmid, we introduced only the U6 promoter onto
927 the pUC19 backbone (pUC19-U6) following the protocol outlined above with these modifications:
928 (i) the U6 promoter was amplified with primers TAAGCA_HindIII_U6_For and
929 TAAGCA_EcoRI_U6_R during the first PCRs and then gel-purified, and (ii) the second and third
930 PCRs were skipped since the promoter was not fused with any other amplicon. The U6 promoter
931 insert on the pUC19 backbone was also sequence verified using Sanger sequencing.

932

933 **Transfections and sample collections for 'omics' analyses**

934 *E. coli* were cultured in LB Broth (Thermo Fisher Scientific) supplemented with 50 μg/mL
935 carbenicillin to an optical density 600 (OD_{600}) of 2 – 4. Plasmid extractions were carried out using
936 the Nucleobond Xtra Midi Plus EF kit (Macherey-Nagel item no. 740422.50) following
937 manufacturer recommendations. Plasmids were aliquoted and stored at -20°C until the time of
938 transfection.

939 On the day of transfection, we washed IMR-90 fibroblasts twice with Dulbecco's
940 phosphate-buffered saline (DPBS, Corning cat. 21-031-CV), detached cells using 0.25% trypsin
941 (HyClone cat. 95053-258), neutralized the trypsin using a two-fold higher volume of media, spun
942 cells down (500xG, 5 minutes), resuspended cells in fresh media, and counted cells by trypan
943 blue staining using a Countess II FL automated cell counter (Thermo Fisher) or a CellDrop

944 Automated Cell Counter (DeNovix). The number of cells necessary for the experiment were then
945 aliquoted, spun down, and washed once with DPBS. Fibroblasts were transfected by
946 electroporation using the Neon Transfection System (Invitrogen) with the following parameters:
947 Buffer R for cell resuspension, 1500 V, 30 ms, and 1 pulse. Per reaction, we maintained a plasmid
948 mass : cell number ratio of 2.5 μg : $2*10^6$ cells. We independently transfected 1.0 – 1.2 * 10^7
949 fibroblasts per 100 mm tissue culture-treated petri dish (GenClone cat. 25-202), preparing 1 – 2
950 dishes to be used for each biological replicate downstream. Immediately after transfection, cells
951 were cultured in Penicillin-Streptomycin-free media and allowed to recover from the
952 electroporation for ~24 hours. Since cell viability following electroporation exhibited plate-to-plate
953 variability, surviving cells were then detached by trypsinization, counted, and re-seeded at equal
954 densities across biological replicates and experimental conditions. We subsequently defined this
955 time point as "0 hours".

956 For paired transcriptomic and proteomic analyses, fibroblasts were prepared following
957 previously described guidelines for generating conditioned media from senescent cells and
958 quiescent control cells (Neri et al., 2021). We implemented this protocol because (i) we
959 hypothesized that *Alu* overexpression may induce senescence-associated changes, based on the
960 published literature, and (ii) this protocol utilizes serum deprivation to restrict proliferation in order
961 to isolate senescent versus non-senescent effects by eliminating non-proliferating vs proliferating
962 effects. More specifically, fibroblasts were independently re-seeded at a density of 6 * 10^6 cells
963 per 150 mm tissue culture-treated dish (Corning cat. 430599), with 5 biological replicates per
964 experimental group. Cells were cultured in 60 mL of 0.2% FBS media, which was replaced after
965 24 hours. At 48 hours, the media was removed, cells were washed twice with DPBS, and cells
966 were fed with 60 mL of FBS-free and phenol red-free MEM media (Corning cat. 17-305-CV)
967 containing Penicillin-Streptomycin-Glutamine and non-essential amino acids. At 72 hours,
968 supernatants were collected in conicals, conicals were spun down (4000xG, 5 minutes, 4°C) to
969 pellet cell debris, and supernatants were processed through Target2 0.45 μm polyvinylidene
970 fluoride (PVDF) syringe filters (Thermo Scientific cat. F2500-5) to remove any remaining cellular
971 debris. Filtered conditioned media was snap frozen in liquid nitrogen and stored at -80°C. Cells
972 were washed with DPBS and detached with 0.05% trypsin (Corning cat. 25-052-CI), trypsin was
973 neutralized with FBS-containing media, and cells were spun down. Cells were washed once with
974 FBS-free and phenol red-free media, spun down, and resuspended again in that same media.
975 Cell viability was assessed by trypan blue staining, ensuring that cell viability > 90% for all
976 samples, and each sample was aliquoted into two tubes, saving 40% of the cells for proteomic

977 analysis and 60% for transcriptomic analysis. Cells were spun down, the supernatants were
978 discarded, and the cell pellets were snap frozen in liquid nitrogen and stored at -80°C. Cellular
979 pellets for transcriptomic analysis were later lysed in TRIzol Reagent (Invitrogen) for downstream
980 total RNA isolation (see below).

981 To ensure that major *Alu*-induced pathway changes replicated in proliferating cells, we
982 prepared additional transcriptomic samples for IMR-90 fibroblasts overexpressing *AluJb* in
983 standard, serum-containing maintenance media. More specifically, fibroblasts were
984 independently transfected as before. Following recovery from the electroporation, fibroblasts were
985 independently re-seeded at a density of 2 – 3 * 10^6 fibroblasts per 100 mm dish containing
986 maintenance media, with 4 biological replicates per experimental group. After 24 hours, cells were
987 lysed in TRIzol Reagent (Invitrogen) for downstream total RNA isolation (see below).

988

989 **RNA extractions and mRNA sequencing**

990 RNA was extracted using the Direct-zol RNA Miniprep kit (Zymo Research cat. R2052) following
991 manufacturer recommendations. To confirm *AluJb* overexpression, complementary DNA (cDNA)
992 was generated for each RNA sample using the Maxima H Minus cDNA Synthesis Master Mix with
993 dsDNase (Thermo Scientific cat. M1682), following manufacturer instructions and including
994 reverse transcriptase negative (RT-) controls. We verified plasmid-specific *AluJb* overexpression
995 by endpoint PCR using MyTaq HS Red Mix (Meridian Bioscience cat. BIO-25048) with primers
996 AluJb_qPCR4 forward/reverse and these PCR settings: initial denaturation (95°C, 1 minute) and
997 35 cycles of denaturation (95°C, 15 seconds), annealing (60°C, 15 seconds), and extension
998 (72°C, 10 seconds). We note that the primers used here were designed to specifically amplify the
999 *AluJb* copy on the overexpression plasmid by targeting the *AluJb* 3'end and the downstream
1000 plasmid backbone sequence.

1001 The integrity of RNA samples was evaluated using an Agilent High Sensitivity RNA
1002 ScreenTape assay (Agilent Technologies). Of the 5 biological replicates per group in the paired
1003 transcriptome/proteome experiment, the 4 samples with the highest eRIN scores, ranging
1004 between 6.2 and 8.8, were selected for sequencing. In the follow-up experiment with standard
1005 serum-containing media, all samples had an eRIN score > 9. We submitted total RNA samples to
1006 Novogene (Sacramento, California) for unstranded mRNA library preparation and sequencing on
1007 the NovaSeq 6000 platform as paired-end 150 bp reads. The raw FASTQ reads have been
1008 deposited to SRA under BioProject PRJNA1008694.

1009

1010 **Protein digestion and desalting**

1011 Frozen cellular pellets and frozen conditioned media were shipped to the USC-Buck
1012 Institute Nathan Shock Center Cellular Senescence and Beyond Core (CSBC) for proteomic
1013 analysis. Conditioned media (30 mL per sample) from either empty vector (N=4) or *Alu*
1014 overexpression (N=4) IMR-90 cultures were concentrated using 3 kDa molecular cut-off filters
1015 (Millipore Sigma, Burlington, MA) and protein concentrations were determined using Bicinchoninic
1016 Acid (BCA) assay (Thermo Fisher Scientific, Waltham, MA). Cell pellets from either empty vector
1017 (N=5) or *Alu* overexpression (N=5) IMR-90 cultures were solubilized in 100 µL of 0.5% sodium
1018 dodecyl sulfate (SDS) in 100 mM Triethylamonium bicarbonate (TEAB) with 1X protease inhibitor
1019 cocktail (PIC). Protein concentrations were determined using BCA assay.

1020 Samples originating from cell pellets (~100 µg) were brought to the same overall volume
1021 of 100 µL with water, while secretome samples (~100 µg) were prepared directly. All samples
1022 were reduced using 20 mM dithiothreitol in 50 mM TEAB at 50°C for 10 minutes, cooled to room
1023 temperature (RT) and held at RT for 10 minutes, and alkylated using 40 mM iodoacetamide in 50
1024 mM TEAB at RT in the dark for 30 minutes. Samples were acidified with 12% phosphoric acid to
1025 obtain a final concentration of 1.2% phosphoric acid. S-Trap buffer consisting of 90% methanol in
1026 100 mM TEAB at pH ~7.1 was added and samples were loaded onto S-Trap mini spin columns
1027 (Protifi). The entire sample volume was spun through the S-Trap mini spin columns at 4,000 x g
1028 and RT, binding the proteins to the micro spin columns. Subsequently, S-Trap micro spin columns
1029 were washed twice with S-Trap buffer at 4,000 x g and RT and placed into clean elution tubes.
1030 Samples were incubated for one-hour at 47°C with sequencing grade trypsin (Promega, San Luis
1031 Obispo, CA) dissolved in 50 mM TEAB at a 1:25 (w/w) enzyme:protein ratio. An additional aliquot
1032 of trypsin dissolved in 50 mM TEAB was added and samples were digested overnight at 37°C.

1033 Peptides were sequentially eluted from mini S-Trap spin columns with 50 mM TEAB, 0.5%
1034 formic acid (FA) in water, and 50% acetonitrile (ACN) in 0.5% FA. After centrifugal evaporation,
1035 samples were resuspended in 0.2% FA in water and desalted with Oasis 10-mg Sorbent
1036 Cartridges (Waters, Milford, MA). The desalted elutions were then subjected to an additional
1037 round of centrifugal evaporation and re-suspended in 0.1% FA in water at a final concentration of
1038 1 µg/µL. Eight microliters of each sample were diluted with 2% ACN in 0.1% FA to obtain a
1039 concentration of 400 ng/µL. One microliter of indexed Retention Time Standard (iRT, Biognosys,
1040 Schlieren, Switzerland) was added to each sample, thus bringing up the total volume to 20 µL
1041 (Escher et al., 2012).

1042

1043 **Mass spectrometric analysis (secretome)**

1044 Reverse-phase high-performance liquid chromatography (HPLC)-MS/MS analyses were
1045 performed on a Dionex UltiMate 3000 system coupled online to an Orbitrap Exploris 480 mass
1046 spectrometer (Thermo Fisher Scientific, Bremen, Germany). The solvent system consisted of 2%
1047 ACN, 0.1% FA in water (solvent A) and 80% ACN, 0.1% FA in ACN (solvent B). Digested peptides
1048 (800 ng) were loaded onto an Acclaim PepMap 100 C_{18} trap column (0.1 x 20 mm, 5 µm particle
1049 size; Thermo Fisher Scientific) over 5 minutes at 5 µL/min with 100% solvent A. Peptides were
1050 eluted on an Acclaim PepMap 100 C_{18} analytical column (75 µm x 50 cm, 3 µm particle size;
1051 Thermo Fisher Scientific) at 300 nL/min using the following gradient: linear from 2.5% to 24.5%
1052 of solvent B in 125 min, linear from 24.5% to 39.2% of solvent B in 40 min, up to 98% of solvent
1053 B in 1 min, and back to 2.5% of solvent B in 1 min. The column was re-equilibrated for 30 min
1054 with 2.5% of solvent B, and the total gradient length was 210 min. Each sample was acquired in
1055 data-independent acquisition (DIA) mode (Bruderer et al., 2017; Collins et al., 2017; Gillet et al.,
1056 2012). Full MS spectra were collected at 120,000 resolution (Automatic Gain Control (AGC)
1057 target: 3e6 ions, maximum injection time: 60 ms, 350-1,650 *m/z*), and MS2 spectra at 30,000
1058 resolution (AGC target: 3e6 ions, maximum injection time: Auto, Normalized Collision Energy
1059 (NCE): 30, fixed first mass 200 *m/z*). The isolation scheme consisted of 26 variable windows
1060 covering the 350-1,650 *m/z* range with an overlap of 1 *m/z* (see **Supplementary Table S2A**)
1061 (Bruderer et al., 2017).

1062

1063 **Mass spectrometric analysis (intracellular protein)**

1064 LC-MS/MS analyses were performed on a Dionex UltiMate 3000 system coupled to an
1065 Orbitrap Eclipse Tribrid mass spectrometer (both from Thermo Fisher Scientific, San Jose, CA).
1066 The solvent system consisted of 2% ACN, 0.1% FA in water (solvent A) and 98% ACN, 0.1% FA
1067 in water (solvent B). Proteolytic peptides (600 ng) were loaded onto an Acclaim PepMap 100 C_{18}
1068 trap column (0.1 x 20 mm, 5-µm particle size; Thermo Fisher Scientific) for 5 min at 5 µL/min with
1069 100% solvent A. Peptides were eluted on an Acclaim PepMap 100 C_{18} analytical column (75 µm
1070 x 50 cm, 3 µm particle size; Thermo Fisher Scientific) at 300 nL/min using the following gradient
1071 of solvent B: 2% for 5 min, linear from 2% to 20% in 125 min, linear from 20% to 32% in 40 min,
1072 up to 80% in 1 min, 80% for 9 min, and down to 2% in 1 min. The column was equilibrated with
1073 2% of solvent B for 29 min, with a total gradient length of 210 min. All samples were acquired in
1074 DIA mode. Full MS spectra were collected at 120,000 resolution (AGC target: 3e6 ions, maximum

injection time: 60 ms, 350-1,650 m/z), and MS2 spectra at 30,000 resolution (AGC target: 3e6 ions, maximum injection time: Auto, NCE: 27, fixed first mass 200 m/z). The isolation scheme consisted of 26 variable windows covering the 350-1,650 m/z range with an overlap of 1 *m/z* (see **Supplementary Table S2A**) (Bruderer et al., 2017).

QUANTIFICATION AND STATISTICAL ANALYSIS

RNA-seq read trimming, mapping, and quantification

Fastq files were first trimmed using fastp v0.20.1 (Chen et al., 2018) to (i) remove adapter sequences, (ii) hard trim the first 15 base pairs of each read to remove biased sequence composition, (iii) remove low quality bases, and (iv) remove reads shorter than 36 base pairs. Read quality for each sample was then inspected using fastqc v0.11.9. Next, the GRCh38 primary human genome assembly and comprehensive gene annotation were obtained from GENCODE release 44 (Frankish et al., 2018). We modified the reference genome to include the sequence for the *AluJb* overexpression plasmid as an additional contig. The trimmed reads were aligned to this modified reference genome using STAR v2.7.3a (Dobin et al., 2012) with the following parameters: outFilterMultimapNmax 100, winAnchorMultimapNmax 100, and outFilterMismatchNoverLmax 0.04. Finally, the TEcount function in the TEtranscripts v2.1.4 (Jin et al., 2015) package was employed to obtain gene and repeat subfamily counts, using the GENCODE annotations to define gene boundaries and a repeat GTF file provided on the Hammell lab website (downloaded on September 14 2023 from https://labshare.cshl.edu/shares/mhammelllab/www-data/TEtranscripts/TE_GTF/GRCh38_GENCODE_rmsk_TE.gtf.gz) to define repeat element boundaries.

Differential gene expression analyses

Gene and repeat subfamily count files were loaded into R v4.3.3. To filter lowly expressed genes in each analysis, a counts-per-million (cpm) threshold corresponding to 10 reads in the median-length library was defined. Genes and repeat subfamilies were kept for analysis if they were expressed at levels surpassing this cpm threshold in at least as many samples as the smallest group. DESeq2 v1.42.1 (Love et al., 2014) was used to identify significant (FDR < 0.05) differentially expressed genes and repeat subfamilies between groups. To visualize sample grouping patterns from the expression data, we carried out multidimensional scaling (MDS)

1107 analysis using a distance metric between samples based on Spearman's rank correlation value
1108 (1-Rho), which was then provided to the 'cmdscale' R function.

1109

1110 **Re-analysis of publicly available transcriptomic data**

1111 We leveraged publicly available mRNA-sequencing data for 133 aging human primary
1112 fibroblast samples (Fleischer et al., 2018) to characterize the effects of aging on the repetitive
1113 element transcriptome. Though others have conducted similar analyses (LaRocca et al., 2020;
1114 Pabis et al., 2024), we applied additional sample processing and filtering criteria to remove batch
1115 effects and isolate aging effects. First, we only kept samples from adults at least 20 years old to
1116 avoid the confounding effects of human development occurring prior to adulthood (leaving 107
1117 samples). We also only kept samples from people who specified 'Caucasian' for their ethnicity
1118 (leaving 95 samples), since this was the most well-represented group, and only kept fibroblast
1119 samples extracted from skin on the arm (leaving 82 samples), to avoid potential confounding
1120 effects from extraction site. Fastq files for the remaining samples were trimmed, mapped, and
1121 quantified as described above, with three modifications: (i) since raw reads were of two different
1122 lengths, the longer reads were hard trimmed with fastp v0.20.1 (Chen et al., 2018) at the 3' end
1123 to ensure that read lengths were equal across all samples, (ii) reads were mapped to the
1124 unmodified human reference genome, and (iii) individual repeat locus counts, in addition to the
1125 repeat subfamily counts, were generated using the TElocal v1.1.1 package and a repeat file
1126 provided on the Hammell lab website (downloaded on October 31 2023
1127 from https://labshare.cshl.edu/shares/mhammelllab/www-data/TElocal/prebuilt_indices/).
1128 Individual repeat locus counts were then aggregated by subfamily and the following genomic
1129 context categories as previously described (Bravo et al., 2024): intronic, exon-overlapping,
1130 intergenic and near a gene (within 5 kilobases), or intergenic and distal from a gene (farther than
1131 5 kilobases).

1132 With the generated counts files, we then checked for potential sample mislabeling or
1133 cross-contamination by checking the expression of the sex-specific markers *XIST* and *DDX3Y*.
1134 Six potential outliers using the 1.5*IQR (interquartile range) rule were omitted from downstream
1135 analyses. This yielded 76 samples that were utilized for differential gene expression analysis
1136 across age, which was carried out as listed above with these alterations: (i) a gene was
1137 considered expressed if it met the cpm threshold in at least 20% of samples and (ii) batch effects
1138 corresponding to biological sex and sequencing instrument were regressed out from the raw read

1139 counts using the 'removeBatchEffect' function in the R package Limma v3.58.1 (Ritchie et al.,
1140 2015).

1141

1142 **DIA-MS Data Processing and Statistical Analysis**

1143 DIA data was processed in Spectronaut (versions 14.10.201222.47784 and
1144 15.1.210713.50606) using directDIA. Data extraction parameters were set as dynamic and non-
1145 linear iRT calibration with precision iRT was selected. Data was searched against the *Homo*
1146 *Sapiens* reference proteome with 20,380 entries (UniProtKB-SwissProt), accessed on
1147 01/29/2021. Trypsin/P was set as the digestion enzyme and two missed cleavages were allowed.
1148 Cysteine carbamidomethylation was set as a fixed modification while methionine oxidation and
1149 protein N-terminus acetylation were set as dynamic modifications. Identification was performed
1150 using 1% precursor and protein q-value. Quantification was based on the peak areas of extracted
1151 ion chromatograms (XICs) of 3 – 6 MS2 fragment ions, specifically b- and y-ions, with q-value
1152 sparse data filtering and iRT profiling applied (**Supplementary Table S2F**). Local normalization
1153 was applied for intracellular protein analysis (i.e., cell pellets), but not for secretome analysis.
1154 Differential protein expression analysis comparing 1) *Alu* overexpression to empty vector was
1155 performed using a paired t-test, and p-values were corrected for multiple testing, using the Storey
1156 method (Burger, 2018). Specifically, group wise testing corrections were applied to obtain q-
1157 values. For intracellular protein analysis, protein groups with at least two unique peptides, q-value
1158 < 0.05, and absolute $\log_2$(fold-change) > 0.2 were called as significantly-altered (**Supplementary**
1159 **Table S2E**). For secretome analysis, protein groups with at least two unique peptides, q-value $<$
1160 0.05, and absolute $\log_2$(fold-change) > 0.58 were called as significantly-altered (**Supplementary**
1161 **Table S2F**).

1162

1163 **Functional enrichment and network analyses**

1164 We used the Gene Set Enrichment Analysis (GSEA) paradigm as implemented in the R
1165 package clusterProfiler v4.10.1 (Wu et al., 2021). Multi-contrast pathway enrichment was also
1166 carried out across "-omics" layers using the mitch v1.14.0 R package (Kaspi and Ziemann, 2020).
1167 Gene Ontology (GO) gene sets were obtained from the Molecular Signature Database release
1168 2024.1.Hs (Liberzon et al., 2015; Subramanian et al., 2005). Reactome v92 pathway gene sets
1169 were obtained directly from the Reactome website (Milacic et al., 2023). We also obtained several
1170 aging- and senescence-associated gene sets, including core senescence-associated secretory

phenotype (SASP) factors (Basisty et al., 2020), SenMayo (Saul et al., 2022), CellAge build 3 (Avelar et al., 2020), aging-related genes derived from the Genotype-Tissue Expression project (Jia et al., 2018), and differentially expressed genes/repeats identified in our analysis of the human aging fibroblast data (Fleischer et al., 2018). Finally, we obtained previously published lists of genes upregulated and downregulated by stable overexpression of *AluSq2* or *AluSx* transposons in IMR-90 fibroblasts (Cantarella et al., 2019). For simplicity, the union of upregulated genes and the union of downregulated genes across both conditions were defined as *AluS* upregulated and downregulated genes, respectively.

For gene set enrichment analysis of transcriptomic changes, the DESeq2 v1.42.1 Wald-statistic was used to generate a ranked list of genes and repeats. For gene set enrichment analysis of proteomic and secretomic changes, the product of the $\log_2$(fold change) and $-\log_{10}$(Q-value) was used to generate a ranked list of proteins, which were then mapped to their corresponding gene symbol. All gene sets with an FDR < 0.05 were considered significant. For plots with a single analysis, the top 5 downregulated and top 5 upregulated gene sets were plotted, at most. For plots with multiple analyses, shared gene sets with consistent expression patterns across individual analyses were first identified. Then, the p-values for shared gene sets were combined using Fisher's method, and this meta-analysis p-value was used to rank shared gene sets. Finally, the top 5 upregulated gene sets and the top 5 downregulated gene sets were plotted, at most. If there were less than 5 gene sets in either group, those were replaced with gene sets exhibiting the opposite regulation, in order to plot 10 shared gene sets whenever possible. For multi-contrast pathway enrichment analysis with mitch, gene sets with an adjusted MANOVA (Multivariate Analysis of Variance) p-value < 0.05 were considered significant. For mosaic plots comparing the abundances of gene set members in differentially versus non-differentially expressed genes/proteins, statistical significance was assessed using Fisher's method, and comparisons with p < 0.05 were considered significantly enriched.

For the transcriptional data, predicted transcription factor activity was inferred using the decoupleR v2.8.0 package (Badia-i-Mompel et al., 2022). The 'fgsea' algorithm was run on the list of genes, and their accompanying Wald statistic, using the CollecTRI curated collection of transcription factors and their targets (Müller-Dott et al., 2023). All regulons with a p < 0.05 were considered significantly differentially impacted, and the top 5 upregulated regulons and the top 5 downregulated regulons by magnitude were plotted. In addition, a gene network was constructed with NetworkAnalyst (Xia et al., 2014; Xia et al., 2015; Zhou et al., 2019) on May 15, 2025. All differentially expressed genes (FDR < 0.05) were ordered by their Wald statistic and submitted to

1204 NetworkAnalyst as a gene list. A network was then constructed by taking the union of a generic
1205 PPI (first order network using the STRING interactome database, 900 confidence score cutoff,
1206 and requiring experimental evidence) and a signaling network (using the SIGNOR 2.0 database).
1207 The most populated subnetwork, subnetwork 1, was then visualized on the platform.

1208

1209 **Functional Assays**

1210 For functional assays, 2-4*10^6 IMR-90 fibroblasts were transfected by electroporation as
1211 previously described and allowed to recover for ~24 hours on 6-well plates. Six independent
1212 transfections per group served as biological replicates in each experiment.

1213

1214 *Metabolic profiling using the Agilent Seahorse platform*

1215 To assess respiratory capacity, cells were detached, and 90,000 cells per well were
1216 seeded on a Seahorse XF Pro M Cell Culture Microplate (Agilent Part No. 103774-100) containing
1217 maintenance media. For each independent transfection, three technical replicate wells were
1218 prepared and cultured for 24 hours. Then, cells were washed and cultured in unbuffered Seahorse
1219 XF base media (Agilent cat. 102353-100) containing 5.5 mM of glucose, and the Seahorse XF
1220 Cell Mito Stress Test (part no. 103015-100) was carried out by the USC Leonard Davis School of
1221 Gerontology Seahorse Core. Afterwards, the media was removed, cells were lysed by freezing at
1222 -80°C overnight, 100 μL of water were added, the plate was placed in a 37°C incubator for 1 hour,
1223 and cells were frozen at -80°C for another hour. After thawing, a 200 μg/mL working solution of
1224 Hoechst 33342 in Tris-NaCl-EDTA (TNE) buffer was prepared, and 100 μL were added per well.
1225 Fluorescence was measured using an excitation wavelength of 346 nm and an emission
1226 wavelength of 460 nm, in order to normalize for cell number differences across wells. This
1227 experiment was repeated twice which yielded n = 12 independent transfection samples per group,
1228 the values were normalized to the median of the control group in each experiment, the values
1229 across experiments were combined, and statistical significance was reached if a Wilcoxon test
1230 yielded $p < 0.05$.

1231

1232 *Cell cycle stage profiling using propidium iodide staining*

1233 Cell cycle status was determined by propidium iodide (PI) staining. After the recovery
1234 period, cells were detached, and ~500,000 - 600,000 cells per well were seeded on 6-well plates
1235 containing maintenance media. After 24 hours, cells were detached, cells were spun down
1236 (300xG, 5 minutes), cells were washed once in DPBS, cells were fixed by drop-wise adding pre-
1237 chilled 70% ethanol, and fixed cells were stored at -20°C for a minimum of 12 hours. Then, cells
1238 were spun down (500xG, 5 minutes, 4°C), cells were washed once with ice-cold DPBS, cells were
1239 resuspended in labeling buffer, and cells were stained for 30 minutes in the dark. Staining buffer
1240 was prepared in DPBS with the following final concentrations: 50 μg/mL propidium iodide (Alfa
1241 Aesar cat. J66584), 100 μg/mL PureLink RNase A (Invitrogen cat. 12091021), and 0.05% Triton
1242 X-100 (MP cat. 194854). This experiment was repeated three times which yielded n = 18
1243 independent transfection samples per group, the values were normalized to the median of the
1244 control group in each experiment, the values across experiments were combined, and statistical
1245 significance was reached if a Wilcoxon test yielded $p < 0.05$.

1246

1247 *Protein aggregation assessment using proteostat staining*

1248 The relative amounts of protein aggregates were determined using the PROTEOSTAT
1249 Aggresome Detection Kit (Enzo cat. No. ENZ-51035-K100). After the recovery period, cells were
1250 detached, and ~500,000 - 600,000 cells per well were seeded on 6-well plates containing
1251 maintenance media. After 24 hours, the assay was carried out, preparing staining solution by
1252 adding Proteostat dye and Hoechst 33342 at a dilution of 1/10,000 and 1/1,000, respectively. This
1253 experiment was repeated four times which yielded n = 24 independent transfection samples per
1254 group, the values were normalized to the median of the control group in each experiment, the
1255 values across experiments were combined, and statistical significance was reached if a Wilcoxon
1256 test yielded $p < 0.05$.

1257 Flow cytometry for Proteostat and cell cycle assays was carried out on a MACSQuant
1258 Analyzer 10 (Miltenyi Biotec, 130-096-343). Flow cytometry data was analyzed in Flowlogic
1259 Solution 1.0.

1260

1261 **Other software versions**

Analyses were conducted using R version 4.3.3 and code was re-run independently on R version 4.3.3 to check for reproducibility. Flow cytometry results were analyzed using Flowlogic Solution 1.0.